Deuterium enriched water ties planet forming disks to comets and protostars

John J. Tobin[1*], Merel L. R. van 't Hoff[2], Margot Leemker[3], Ewine F. van Dishoeck[3], Teresa Paneque-Carreño[3,4], Kenji Furuya[5], Daniel Harsono[6], Magnus V. Persson[7], L. Ilsedore Cleeves[8], Patrick D. Sheehan[9] and Lucas Cieza[10,11]

[1*]National Radio Astronomy Observatory, 520 Edgemont Rd., Charlottesville, 22903, VA, USA.
[2]Department of Astronomy, University of Michigan, 1085 S. University Ave., Ann Arbor, 48109, MI, USA.
[3]Leiden Observatory, Leiden University, P.O. Box 9513, Leiden, 2300-RA, The Netherlands.
[4]European Southern Observatory, Karl-Schwarzschild-Str 2, Garching, 85748, Germany.
[5]National Astronomical Observatory of Japan, Osawa 2-21-1, Mitaka, Tokyo, 181-8588, Japan.
[6]Institute of Astronomy, Department of Physics, National Tsing Hua University, Hsinchu, Taiwan.
[7]Department of Space, Earth and Environment, Chalmers University of Technology, Onsala Space Observatory, Onsala, 43992, Sweden.
[8]Department of Astronomy, University of Virginia, 530 McCormick Rd., Charlottesville, 22904, VA, USA.
[9]Center for Interdisciplinary Exploration and Research in Astronomy, Northwestern University, 1800 Sherman Rd., Evanston, 60202, IL, USA.
[10]Núcleo de Astronomía, Facultad de Ingeniería y Ciencias, Universidad Diego Portales, Av. Ejercito 441, Santiago, Chile.
[11]Millennium Nucleus on Young Exoplanets and their Moons (YEMS), Universidad Diego Portales, Av. Ejercito 441, Santiago, Chile.

*Corresponding author(s). E-mail(s): jtobin@nrao.edu;

Keywords: proto-planetary disks, water chemistry

Water is a fundamental molecule in the star and planet formation process, essential for catalyzing the growth of solid material and the formation of planetesimals within disks [1, 2]. However, the water snowline and the HDO/H_2O ratio within proto-planetary disks have not been well-characterized because water only sublimates at ∼160 K [3], meaning that most water is frozen-out onto dust grains and the water snowline radii are <10 au [4, 5]. The sun-like protostar V883 Ori (M_*=1.3 $M_\odot$) [6], is undergoing an accretion burst [7], increasing its luminosity to ∼200 $L_\odot$ [8] and previous observations suggested that its water snowline is 40-120 au in radius [6, 9, 10]. Here we report the direct detection of gas phase water (HDO and $H_2{}^{18}O$) from the disk of V883 Ori. We measure a midplane water snowline radius of ∼80 au, comparable to the scale of the Kuiper Belt, and water is detected out to a radius of ∼160 au. We then measure the HDO/H_2O ratio of the disk to be $(2.26 \pm 0.63)\times10^{-3}$. This ratio is comparable to protostellar envelopes, comets, and exceeds that of Earth's oceans by 3.1σ. We conclude that disks directly inherit water from the star-forming cloud and this water becomes incorporated into large icy bodies, like comets, without significant chemical alteration.

We observed V883 Ori (located within the Orion molecular clouds) using the Atacama Large Millimeter/submillimeter Array (ALMA) at ∼0.″1 resolution (40 au diameter at its distance of ∼400 pc [11]). The full extent of the proto-planetary disk surrounding V883 Ori is well-resolved in our observations, with the dust and gas emission extending to ∼125 au and 320 au, respectively [6]. The disk around V883 Ori is young, similar to the well-known HL Tau system [12], and the disk mass of 0.02∼0.09 $M_\odot$ is ∼10× greater than the surrounding envelope mass [6, 13]. The accretion burst (which may have begun more than 130 yr ago [7, 14]) has heated a large fraction of the disk above the sublimation temperature of water, and we illustrate how V883 Ori and a more typical proto-planetary disk differ in Figure 1.

We detect three emission lines of gas phase water within the disk of V883 Ori: HDO at 225.89672 and 241.561550 GHz and $H_2{}^{18}O$ at 203.40752 GHz (see Methods section). The HDO and $H_2{}^{18}O$ kinematics are consistent with Keplerian rotation (see Extended Data Figures 1 and 2). The emission from all three lines peak at a radius of 50 to 60 au, but extend to ∼160 au (Figure 2 and Extended Data Figure 3). HDO is significantly brighter than $H_2{}^{18}O$ (despite the D/H ratio <1) owing to the ratio of $^{16}O/^{18}O$ and its molecular properties (see Methods section). The structure and extent of the water emission is very similar to complex organic molecules (COMs), like methanol [9, 15], which makes sense given that methanol is expected to sublimate at a similar temperature (∼130 K) [3]. $C^{17}O$, however, is more extended than water and methanol because it sublimates at ∼25 K [16], (Figure 2). The apparent depression of emission in the center of some images in Figure 2 is due to the opacity of the continuum, absorbing gas emission at radii <40 au. The

high dust optical depth at smaller radii, even for more-evolved disks [17], may obscure molecular line emission coming from the disk midplane and make the midplane water emission of lower luminosity systems difficult to characterize.

The warm nature of V883 Ori's disk enables us to characterize its water reservoir with spatially-resolved observations, unlike most proto-planetary disks (Figure 1) [18]. We measured the column densities of HDO and $H_2{}^{18}O$ in several ways to test the robustness of our measurements (see Methods section). For our primary method, we extracted the integrated spectra within a 0.″4 (160 au) radius to measure the total flux of the emission lines (see Extended Data Figure 4). We also extracted radial intensity profiles from the integrated intensity maps in Figure 2 using Keplerian Masks. The spectral extraction method yields a disk-averaged measurement, while the integrated intensity method yields the measurements as a function of disk radius. The integrated fluxes of the HDO lines are 0.644±0.028 and 0.595±0.037 Jy km $s^{-1}$for the 225 and 241 GHz lines, respectively, while the $H_2{}^{18}O$ line flux is 0.126±0.025 Jy km s^{-1}.

The ratio of the upper level column densities for the two HDO lines is used to estimate the water excitation temperature (199±42 K). This temperature is used to derive the column densities for HDO and $H_2{}^{18}O$ of (6.98 ± 1.15)×10^{15} cm^{-2} and (5.52 ± 1.13)×10^{15} cm^{-2}, respectively. The $H_2{}^{18}O$ column density translates to a H_2O column density of (3.09 ± 0.70)×10^{18} cm^{-2} (see Methods section). The radial column density profiles of HDO and $H_2{}^{18}O$ are shown in Figure 3 and are consistent with the disk-averaged measurements. The midplane water snowline is estimated to be ∼80 au, corresponding to the radius where the HDO and $H_2{}^{18}O$ column density begins to rapidly decline (Figure 3). The total gaseous water mass in the disk is 1.69×10^{27} g, equivalent to ∼1200 Earth oceans. This is a lower limit because it does not include water at radii <40 au or the water ice in the outer disk. Finally, we calculate a disk-averaged HDO/H_2O ratio of (2.26 ± 0.63)×10^{-3}, consistent with the HDO/H_2O radial profile (Figure 3). The measurements of the HDO/H_2O ratios from different methods are all consistent within their their 1 s.d. uncertainties, demonstrating that the measurement method does not strongly influence the results (see Extended Data Table 4).

Water (H_2O, HDO, and D_2O) is expected to form as ice mantles on dust grains in the cold interstellar medium (ISM) via grain surface reactions. The abundance of deuterated species becomes enhanced in the cold ISM due to deuterium becoming locked into H_2D^+, and the dissociative recombination of deuterium bearing molecules increases the free deuterium available for HDO and D_2O formation within ice mantles [18, 19]. The HDO/H_2O ratio in ice mantles is not well-constrained, only upper limits of ∼10^{-2} are available [20]. However, within the warm gas at small radii around Class 0 protostars, where these ices have sublimated, the HDO/H_2O ratios are found to be between ∼6×10^{-4} to 2×10^{-3} [21–23]. Then comets range from 3×10^{-4} to 10^{-3} [24, 25], and Earth's oceans are 3.11×10^{-4} (see Extended Data Table 5). The

HDO/H_2O ratio for V883 Ori and these different objects are summarized in Figure 4.

The HDO/H_2O ratio of V883 Ori is comparable to the youngest (Class 0) protostars [22], and then compared to more-evolved objects that formed within the Solar System, V883 Ori's HDO/H_2O ratio is also similar to many Oort Cloud comets and 67P from the Jupiter Family Comets (Figure 4). This makes sense because comets are icy relics that are expected to have formed in the outer parts of the proto-planetary disk. It is important to note that it was previously thought that the Jupiter Family and Oort cloud comets formed at different locations in the Solar System, close to the orbits of the giant planets and outside the orbit of Neptune, respectively. It is now thought that the populations are mixed [26], but their HDO/H_2O ratios should reflect their original formation location. However, Earth's oceans and some comets have a lower HDO/H_2O compared to V883 Ori, implying that the water in those bodies may have undergone further processing at high temperatures, lowering their HDO/H_2O ratios. Or, the HDO/H_2O ratio is intrinsically lower in the bodies responsible for water delivery to Earth.

Indeed, it has been shown that outbursts can lower the HDO/H_2O ratio in the inner 1 to 3 au of a disk via a combination of high gas temperature (>500 K), radial mixing, and isotope exchange reactions in the gas phase ($HDO + H_2 \rightarrow H_2O + HD$) [27]. However, this fast evolution of the gaseous HDO/H_2O ratio is only taking place at radii smaller than we can probe in V883 Ori (and inside the optically thick dust). Conversely, at radii >10 au, the lower temperature (200-300 K) and densities mean that the isotope exchange reactions are extremely slow; it would take >100 Myr to significantly change the observed HDO/H_2O ratio in V883 Ori [28]. This means that V883 Ori's HDO/H_2O ratio is tracing that of water sublimated from the ices. The slowness of the isotope exchange reactions and the fact that HDO is only efficiently created in ice, means that the water emission in V883 Ori, even if it is coming from upper layers of the disk (Figure 1), is expected to have a similar HDO/H_2O ratio to the disk midplane.

The HDO/H_2O ratio within the disk of V883 Ori, at the end of the protostar phase, fills in a crucial gap in the water trail just prior to or contemporaneous with the formation of large solid bodies within the disk. The relative constancy of the HDO/H_2O ratio from the protostar phase to the protoplanetary disk implies that the water within the disk of V883 Ori is directly inherited from the infalling envelope [29–31]. Furthermore, the comet 67P, protostars, and V883 Ori [15] all have CH_2DOH/CH_3OH ratios that are $\sim$10$\times$ their HDO/H_2O ratios. This is further evidence that both water and methanol (and the deuterated species) are formed on icy dust grains, that the molecules are inherited from the pre-stellar phase, and that significant chemical reset does not occur during disk or comet formation. Some chemical changes are observed from the envelope to disk [32], but the effect is not strong enough to impact the water and likely other COMs that arrive to the disk as ice [33, 34]. While the specific delivery mechanism of water on Earth remains debated

(comets and/or asteroids) [35], the high D/H found in V883 Ori is evidence that the water molecules in our Solar System originated in the cold interstellar medium, prior to the formation of the Sun [29]. Therefore, spatially-resolved water observations toward young planet forming disks are crucial in linking the water reservoir and the formation of terrestrial planets.

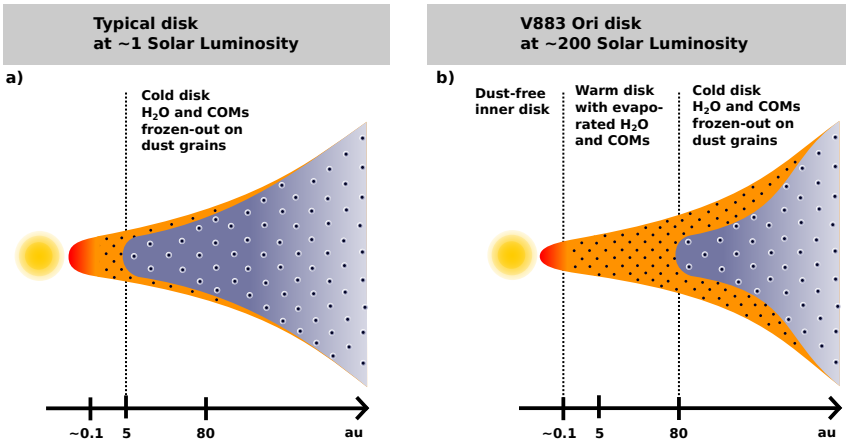

Fig. 1 Illustrations comparing a typical proto-planetary disk and the disk surrounding the outbursting protostar V883 Ori. The panel a) illustrates a typical disk where water and complex organic molecules (COMs) are frozen-out onto dust grains at most radii except the very inner disk. Panel b) illustrates the case of V883 Ori where the disk has a much larger region where water and COMs are sublimated from the dust grains, enabling the water and COM emission to be detected and resolved. Orange and red regions denote the warmer regions of the disk where the ices are sublimated and the light blue/gray denotes the colder regions where the water and COMs are frozen-out. The black points alone denote dust grains with no ice coating, while the black points with gray circles around them denote icy dust grains.

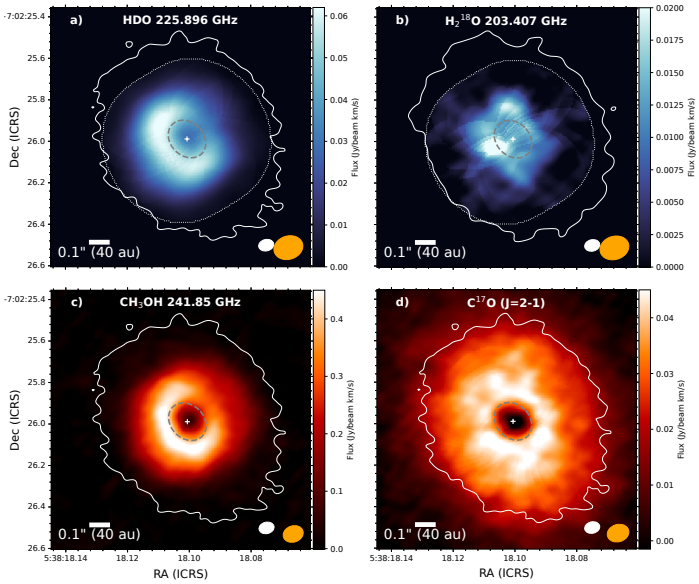

Fig. 2 Integrated intensity images of water and other molecular lines in the disk of V883 Ori. We show the HDO 225 GHz line (a), the $H_2{}^{18}O$ 203 GHz line (b), CH_3OH (c), and $C^{17}O$ (d), as the color scale, while the outer extent of the dust continuum emission is shown as a white contour; the dotted line in panel a) shows the region over which the integrated intensity image was computed using the Keplerian mask. The white cross marks the location of the continuum emission peak and the position of the protostar. The HDO and $H_2{}^{18}O$ lines show emission that is smaller in radial extent than the continuum and $C^{17}O$ emission. The CH_3OH (methanol) image shows a very similar structure and extent relative to the HDO and $H_2{}^{18}O$ lines. $C^{17}O$ more fully traces the extent of the disk gas emission with its lower sublimation temperature of $\sim$25 K, extending beyond the continuum emission. The central depression in emission for all lines is the result of optically thick continuum emission attenuating the molecular emission at radii smaller than $\sim$40 au ($0\farcs1$); the extent of this optically thick region is denoted with the dashed thick gray line in the center of each image. The depression is less obvious for $H_2{}^{18}O$ in panel (b) due to its lower S/N and some contamination of its integrated intensity map from a neighboring line. The ellipses in the lower right corner denote the resolution of the line observations (orange, $\sim$0.1″) and the continuum (white, $\sim0\farcs08$).

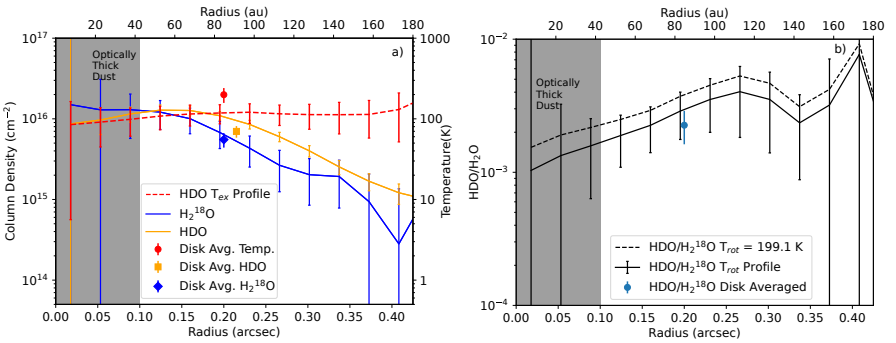

Fig. 3 Radial column density measurements of water and the HDO/H_2O ratio along with their disk-averaged measurements. The radial column density profiles of HDO and $H_2{}^{18}O$ are shown in panel (a) and the HDO/H_2O ratio as a function of deprojected radius in the disk of V883 Ori is shown in panel (b). The disk-averaged values are plotted at 0.″2 in both panels. The HDO column density is the average of the column density derived from the two HDO transitions (this only reduces the uncertainties because the HDO column density will be identical for the two transitions). The HDO column densities have some contamination from a neighboring COM line for the 241 GHz transition, which has been quantified in the Methods Section. This contamination could affect the temperature and the HDO/H_2O profile, but the overall effect is small as shown by the agreement with the disk-averaged value, which has has the contamination of the HDO 241 GHz line removed. The same excitation temperature profile derived from the HDO radial intensity profiles (panel a), red dashed line) is used to calculate both the HDO and $H_2{}^{18}O$ column density profiles (see Methods). The HDO/H_2O ratio calculated with a fixed, 199 K, excitation temperature is shown as the dashed line, and the solid line uses the HDO excitation temperature profile. The error bars are only shown on the solid line for clarity, but are similar for a constant excitation temperature. The uncertainties drawn correspond to 1 s.d. in the measurements from standard error propagation. We shade the radius <0.″1 (40 au) where the disk is optically thick and the measurements are unreliable.

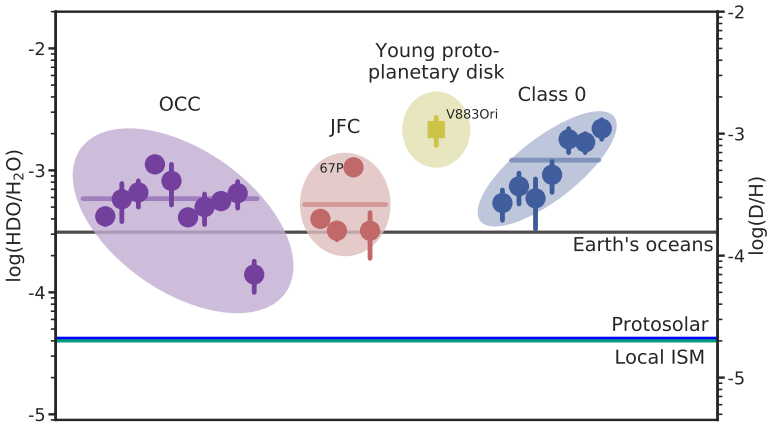

Fig. 4 HDO/H_2O ratio for Class 0 protostars, V883 Ori, Jupiter Family comets (JFC, with 67P labeled), Oort Cloud comets (OCC), Earth's oceans, the Sun, and the local interstellar medium (ISM). The points are arranged to highlight a potential evolutionary scenario with the forming protostars on the right, the 'evolved' Solar System bodies on the left, and V883 Ori fills in a region of parameter space for a young proto-planetary disk, just prior to or contemporaneous with planet formation. The ellipses drawn around the different groups are meant to guide the eye, but the horizontal lines within each ellipse denote the mean HDO/H_2O ratio for each group, and the vertical lines associated with each point represent the 1 s.d. uncertainties. If a vertical line is not visible, the uncertainty is less than the size of the symbol. In the context of other measurements, V883 Ori indicates that the HDO/H_2O ratio does not strongly evolve from the protostar phase to the disk, providing further observational evidence that the water is directly inherited from the envelope to the disk without significant chemical changes. Moreover, the HDO/H_2O ratio of comets are similar to V883 Ori (but slightly below), indicating that the water we probe in the gas phase within the disk of V883 Ori is similar to the water that becomes incorporated into comets. The individual measurements are tabulated in the Methods section (Extended Data Table 5.)

References

[1] J. Blum and G. Wurm. The growth mechanisms of macroscopic bodies in protoplanetary disks. *ARA&A*, 46:21–56, 2008.

[2] Satoshi Okuzumi, Hidekazu Tanaka, Hiroshi Kobayashi, and Koji Wada. Rapid Coagulation of Porous Dust Aggregates outside the Snow Line: A Pathway to Successful Icy Planetesimal Formation. *Astrophys. J.*, 752(2):106, 2012.

[3] E. M. Penteado, C. Walsh, and H. M. Cuppen. Sensitivity Analysis of Grain Surface Chemistry to Binding Energies of Ice Species. *Astrophys. J.*, 844(1):71, 2017.

[4] M. Lecar, M. Podolak, D. Sasselov, and E. Chiang. On the Location of the Snow Line in a Protoplanetary Disk. *Astrophys. J.*, 640(2):1115–1118, 2006.

[5] John S. Carr, Joan R. Najita, and Colette Salyk. Measuring the Water Snow Line in a Protoplanetary Disk. *Research Notes of the American Astronomical Society*, 2(3):169, 2018.

[6] Lucas A. Cieza, Simon Casassus, John Tobin, Steven P. Bos, Jonathan P. Williams, Sebastian Perez, Zhaohuan Zhu, Claudio Caceres, Hector Canovas, Michael M. Dunham, Antonio Hales, Jose L. Prieto, David A. Principe, Matthias R. Schreiber, Dary Ruiz-Rodriguez, and Alice Zurlo. Imaging the water snow-line during a protostellar outburst. *Nature*, 535(7611):258–261, 2016.

[7] Karen M. Strom and Stephen E. Strom. The Discovery of Two FU Orionis Objects in L1641. *Astrophys. J. L.*, 412:L63, 1993.

[8] E. Furlan, W. J. Fischer, B. Ali, A. M. Stutz, T. Stanke, J. J. Tobin, S. T. Megeath, M. Osorio, L. Hartmann, N. Calvet, C. A. Poteet, J. Booker, P. Manoj, D. M. Watson, and L. Allen. The Herschel Orion Protostar Survey: Spectral Energy Distributions and Fits Using a Grid of Protostellar Models. *Astrophys. J. Supp.*, 224(1):5, 2016.

[9] Merel L. R. van 't Hoff, John J. Tobin, Leon Trapman, Daniel Harsono, Patrick D. Sheehan, William J. Fischer, S. Thomas Megeath, and Ewine F. van Dishoeck. Methanol and its Relation to the Water Snowline in the Disk around the Young Outbursting Star V883 Ori. *Astrophys. J. L.*, 864(1):L23, 2018.

[10] M. Leemker, M. L. R. van't Hoff, L. Trapman, M. L. van Gelder, M. R. Hogerheijde, D. Ruíz-Rodríguez, and E. F. van Dishoeck. Chemically tracing the water snowline in protoplanetary disks with HCO^+. *Astron.*

Astrophys., 646:A3, 2021.

[11] Marina Kounkel, Kevin Covey, Genaro Suárez, Carlos Román-Zúñiga, Jesus Hernandez, Keivan Stassun, Karl O. Jaehnig, Eric D. Feigelson, Karla Peña Ramírez, Alexandre Roman-Lopes, Nicola Da Rio, Guy S. Stringfellow, J. Serena Kim, Jura Borissova, José G. Fernández-Trincado, Adam Burgasser, D. A. García-Hernández, Olga Zamora, Kaike Pan, and Christian Nitschelm. The APOGEE-2 Survey of the Orion Star-forming Complex. II. Six-dimensional Structure. *Astron. J.*, 156(3):84, 2018.

[12] ALMA Partnership, C. L. Brogan, L. M. Pérez, T. R. Hunter, W. R. F. Dent, A. S. Hales, R. E. Hills, S. Corder, E. B. Fomalont, C. Vlahakis, Y. Asaki, D. Barkats, A. Hirota, J. A. Hodge, C. M. V. Impellizzeri, R. Kneissl, E. Liuzzo, R. Lucas, N. Marcelino, S. Matsushita, K. Nakanishi, N. Phillips, A. M. S. Richards, I. Toledo, R. Aladro, D. Broguiere, J. R. Cortes, P. C. Cortes, D. Espada, F. Galarza, D. Garcia-Appadoo, L. Guzman-Ramirez, E. M. Humphreys, T. Jung, S. Kameno, R. A. Laing, S. Leon, G. Marconi, A. Mignano, B. Nikolic, L. A. Nyman, M. Radiszcz, A. Remijan, J. A. Rodón, T. Sawada, S. Takahashi, R. P. J. Tilanus, B. Vila Vilaro, L. C. Watson, T. Wiklind, E. Akiyama, E. Chapillon, I. de Gregorio-Monsalvo, J. Di Francesco, F. Gueth, A. Kawamura, C. F. Lee, Q. Nguyen Luong, J. Mangum, V. Pietu, P. Sanhueza, K. Saigo, S. Takakuwa, C. Ubach, T. van Kempen, A. Wootten, A. Castro-Carrizo, H. Francke, J. Gallardo, J. Garcia, S. Gonzalez, T. Hill, T. Kaminski, Y. Kurono, H. Y. Liu, C. Lopez, F. Morales, K. Plarre, G. Schieven, L. Testi, L. Videla, E. Villard, P. Andreani, J. E. Hibbard, and K. Tatematsu. The 2014 ALMA Long Baseline Campaign: First Results from High Angular Resolution Observations toward the HL Tau Region. *Astrophys. J. L.*, 808(1):L3, 2015.

[13] Patrick D. Sheehan, John J. Tobin, Leslie L. Looney, and S. Thomas Megeath. The VLA/ALMA Nascent Disk and Multiplicity (VANDAM) Survey of Orion Protostars VI. Insights from Radiative Transfer Modeling. *arXiv e-prints*, page arXiv:2203.00029, 2022.

[14] Edward Charles Pickering. Detection of new nebulae by photography. *Annals of Harvard College Observatory*, 18(6):113–117, 1890.

[15] Jeong-Eun Lee, Seokho Lee, Giseon Baek, Yuri Aikawa, Lucas Cieza, Sung-Yong Yoon, Gregory Herczeg, Doug Johnstone, and Simon Casassus. The ice composition in the disk around V883 Ori revealed by its stellar outburst. *Nature Astronomy*, 3:314–319, 2019.

[16] Mark P. Collings, Mark A. Anderson, Rui Chen, John W. Dever, Serena Viti, David A. Williams, and Martin R. S. McCoustra. A laboratory survey of the thermal desorption of astrophysically relevant molecules.

Mon. Not. R. Astron. Soc., 354(4):1133–1140, 2004.

[17] Sean M. Andrews, D. J. Wilner, A. M. Hughes, Chunhua Qi, and C. P. Dullemond. Protoplanetary Disk Structures in Ophiuchus. II. Extension to Fainter Sources. *Astrophys. J.*, 723(2):1241–1254, 2010.

[18] E. F. van Dishoeck, L. E. Kristensen, J. C. Mottram, A. O. Benz, E. A. Bergin, P. Caselli, F. Herpin, M. R. Hogerheijde, D. Johnstone, R. Liseau, B. Nisini, M. Tafalla, F. F. S. van der Tak, F. Wyrowski, A. Baudry, M. Benedettini, P. Bjerkeli, G. A. Blake, J. Braine, S. Bruderer, S. Cabrit, J. Cernicharo, Y. Choi, A. Coutens, Th. de Graauw, C. Dominik, D. Fedele, M. Fich, A. Fuente, K. Furuya, J. R. Goicoechea, D. Harsono, F. P. Helmich, G. J. Herczeg, T. Jacq, A. Karska, M. Kaufman, E. Keto, T. Lamberts, B. Larsson, S. Leurini, D. C. Lis, G. Melnick, D. Neufeld, L. Pagani, M. Persson, R. Shipman, V. Taquet, T. A. van Kempen, C. Walsh, S. F. Wampfler, U. Yıldız, and WISH Team. Water in star-forming regions: physics and chemistry from clouds to disks as probed by Herschel spectroscopy. *Astron. Astrophys.*, 648:A24, 2021.

[19] A. G. G. M. Tielens. Surface chemistry of deuterated molecules. *Astron. Astrophys.*, 119(2):177–184, 1983.

[20] B. Parise, T. Simon, E. Caux, E. Dartois, C. Ceccarelli, J. Rayner, and A. G. G. M. Tielens. Search for solid HDO in low-mass protostars. *Astron. Astrophys.*, 410:897–904, 2003.

[21] M. V. Persson, J. K. Jørgensen, E. F. van Dishoeck, and D. Harsono. The deuterium fractionation of water on solar-system scales in deeply-embedded low-mass protostars. *Astron. Astrophys.*, 563:A74, 2014.

[22] S. S. Jensen, J. K. Jørgensen, L. E. Kristensen, K. Furuya, A. Coutens, E. F. van Dishoeck, D. Harsono, and M. V. Persson. ALMA observations of water deuteration: a physical diagnostic of the formation of protostars. *Astron. Astrophys.*, 631:A25, 2019.

[23] S. S. Jensen, J. K. Jørgensen, L. E. Kristensen, A. Coutens, E. F. van Dishoeck, K. Furuya, D. Harsono, and M. V. Persson. ALMA observations of doubly deuterated water: inheritance of water from the prestellar environment. *Astron. Astrophys.*, 650:A172, 2021.

[24] K. Altwegg, H. Balsiger, A. Bar-Nun, J. J. Berthelier, A. Bieler, P. Bochsler, C. Briois, U. Calmonte, M. Combi, J. De Keyser, P. Eberhardt, B. Fiethe, S. Fuselier, S. Gasc, T. I. Gombosi, K. C. Hansen, M. Hässig, A. Jäckel, E. Kopp, A. Korth, L. LeRoy, U. Mall, B. Marty, O. Mousis, E. Neefs, T. Owen, H. Rème, M. Rubin, T. Sémon, C. Y. Tzou, H. Waite, and P. Wurz. 67P/Churyumov-Gerasimenko, a Jupiter family comet with a high D/H ratio. *Science*, 347(6220):1261952, 2015.

[25] Kathrin Altwegg, Hans Balsiger, and Stephen A. Fuselier. Cometary Chemistry and the Origin of Icy Solar System Bodies: The View After Rosetta. *ARA&A*, 57:113–155, 2019.

[26] K. Altwegg, H. Balsiger, J. J. Berthelier, A. Bieler, U. Calmonte, J. De Keyser, B. Fiethe, S. A. Fuselier, S. Gasc, T. I. Gombosi, T. Owen, L. Le Roy, M. Rubin, T. Sémon, and C. Y. Tzou. D_2O and HDS in the coma of 67P/Churyumov-Gerasimenko. *Philosophical Transactions of the Royal Society of London Series A*, 375(2097):20160253, 2017.

[27] James E. Owen and Emmanuel Jacquet. Astro- and cosmochemical consequences of accretion bursts - I. The D/H ratio of water. *Mon. Not. R. Astron. Soc.*, 446(4):3285–3296, 2015.

[28] Christine Lécluse and François Robert. Hydrogen isotope exchange reaction rates: Origin of water in the inner solar system. *Geochimica et Cosmochimica Acta*, 58(13):2927–2939, 1994.

[29] L. Ilsedore Cleeves, Edwin A. Bergin, Conel M. O. 'D. Alexander, Fujun Du, Dawn Graninger, Karin I. Öberg, and Tim J. Harries. The ancient heritage of water ice in the solar system. *Science*, 345(6204):1590–1593, 2014.

[30] K. Furuya, E. F. van Dishoeck, and Y. Aikawa. Reconstructing the history of water ice formation from HDO/H_2O and D_2O/HDO ratios in protostellar cores. *Astron. Astrophys.*, 586:A127, 2016.

[31] K. Furuya, M. N. Drozdovskaya, R. Visser, E. F. van Dishoeck, C. Walsh, D. Harsono, U. Hincelin, and V. Taquet. Water delivery from cores to disks: Deuteration as a probe of the prestellar inheritance of H_2O. *Astron. Astrophys.*, 599:A40, 2017.

[32] Nami Sakai, Takeshi Sakai, Tomoya Hirota, Yoshimasa Watanabe, Cecilia Ceccarelli, Claudine Kahane, Sandrine Bottinelli, Emmanuel Caux, Karine Demyk, Charlotte Vastel, Audrey Coutens, Vianney Taquet, Nagayoshi Ohashi, Shigehisa Takakuwa, Hsi-Wei Yen, Yuri Aikawa, and Satoshi Yamamoto. Change in the chemical composition of infalling gas forming a disk around a protostar. *Nature*, 507(7490):78–80, 2014.

[33] R. Visser, E. F. van Dishoeck, S. D. Doty, and C. P. Dullemond. The chemical history of molecules in circumstellar disks. I. Ices. *Astron. Astrophys.*, 495(3):881–897, 2009.

[34] Maria N. Drozdovskaya, Catherine Walsh, Ruud Visser, Daniel Harsono, and Ewine F. van Dishoeck. Methanol along the path from envelope to protoplanetary disc. *Mon. Not. R. Astron. Soc.*, 445(1):913–929, 2014.

[35] David P. O'Brien, Andre Izidoro, Seth A. Jacobson, Sean N. Raymond, and David C. Rubie. The Delivery of Water During Terrestrial Planet Formation. *Space Sci. Rev.*, 214(1):47, 2018.

1 Methods

V883 Ori was observed with the Atacama Large Millimeter/submillimeter Array (ALMA) located on llano de Chajnantor in Northern Chile in 2021 November. Observations were conducted in Band 6 (∼1.3 mm) and Band 5 (∼1.5 mm) to target the HDO and $H_2{}^{18}O$ spectral lines, respectively.

1.1 Band 5 Observations

The Band 5 observations were conducted with two executions on 2021 November 03 and 04 during C-7 configuration with a maximum baseline length of ∼3000 kλ, with a precipitable water vapor (pwv) of 0.72 and 0.78 mm, respectively. There were 41 antennas operating during the first execution and 43 during the second. Each execution was ∼80 minutes in duration with ∼38 minutes on source per execution for a total time on source in Band 5 of ∼76 minutes. The monitored quasar J0538-4405 was the absolute flux density and bandpass calibrator in the first execution and J0423-0120 was the flux density and bandpass calibrator in the second execution. Both executions used J0541-0541 as the phase calibrator. The central frequency of the observations was ∼195.8 GHz and we simultaneously observed many molecular transitions (see Extended Data Table 1), but our main focus in this paper is the $H_2{}^{18}O$ transition at 203.40752 GHz. The absolute flux density uncertainty in Band 5 is expected to be ∼5%.

1.2 Band 6 Observations

The Band 6 observations were conducted in two consecutive executions on 2021 November 01 during C-7 configuration with a maximum baseline length of ∼4000 kλ. The measured pwv values were 0.74 and 0.77 mm. There were 48 antennas operating during both executions and each execution was ∼75 minutes in duration with ∼40.5 minutes on-source, yielding a total time on source in Band 6 of ∼81 minutes. Both executions used J0423-0120 as the absolute flux density and bandpass calibrator and J0541-0541 as the phase calibrator. The absolute flux density uncertainty in Band 6 is expected to be ∼5%. The central frequency of the observations was ∼233.5 GHz and we simultaneously observed many molecular transitions (see Extended Data Table 1), but our main focus in this paper is the two HDO transitions at 225.89672 and 241.5615499 GHz. However, we compare to the methanol (CH_3OH) transitions observed in a separate spectral window with high spectral resolution.

1.3 Data Reduction

The data were reduced using the ALMA calibration pipeline within CASA 6.2.1 [36]. We used the pipeline-calibrated visibility data and the continuum regions identified by the ALMA pipeline task *hif_findcont* to perform self-calibration on the continuum data and applying the phase and amplitude solutions to the line data as well. Continuum subtraction was also performed using the line-free continuum regions for fitting the underlying continuum using the CASA task *uvcontsub*.

The HDO line at 225 GHz was imaged with the CASA task *tclean* using a robust parameter of 2.0, a channel spacing of 0.162 km s^{-1}, an image size of 768×768, and a pixel size of 0.″0075. All the images used the modified Briggs weighting scheme, set with the *tclean* parameter *weighting='briggsbwtaper'*. The resulting beam was 0.″104×0.″082. Then the HDO line at 241 GHz was created using the same image parameters, but with a channel spacing of 0.151 km s^{-1} and a beam of 0.″098×0.″077. The $H_2{}^{18}O$ line at 203 GHz was imaged with the same parameters as the HDO lines, but with a channel spacing of 0.4 km s^{-1} due to the lower S/N of the line emission as compared to the HDO lines; the beamsize for $H_2{}^{18}O$ is 0.″14×0.″11. The other data cubes, including methanol, were created using the same parameters and their native channel spacing (Extended Data Table 1). To facilitate consistency in the analysis, we generated cubes for each HDO transition that use the same restoring beam as the $H_2{}^{18}O$ cube and 0.4 km s^{-1} channels. This provides for a more consistent comparison of the derived radial profiles for HDO and $H_2{}^{18}O$ and we use these data with the same channel width and restoring beams exclusively for analysis of the HDO/H_2O ratio. Finally, aggregate continuum images were created for the Band 5 and Band 6 data individually, using the line-free regions from all the spectral windows in each band combined. These continuum images had the same image and pixel sizes as the cubes. The synthesized beams of the Band 5 and Band 6 continuum images are 0.″11×0.″088 and 0.″073×0.″055, respectively.

1.4 Analysis

1.4.1 Keplerian Masks

The presence of other strong emission lines from COMs preclude a simple extraction of spectral line fluxes from the disk of V883 Ori. It is known that $H_2{}^{18}O$ can be contaminated by nearby CH_3OCH_3 (dimethyl ether) lines, and HDO at 225 GHz can be contaminated by CH_3OCHO (methyl formate) [21, 22]. Furthermore, HDO at 241 GHz also has contamination, which is likely to come from CH_3CHO (acetalaldehyde). Thus, we use Keplerian masks to isolate the HDO and $H_2{}^{18}O$ emission as best as possible. Keplerian masks select areas within particular channels of a data cube where emission from a Keplerian disk is expected, based on the known mass of the protostar. We make use of a Keplerian mask implementation [37] where various parameters (e.g., stellar mass, disk radius, system velocity, emitting height, line width, etc.) can be

tuned to optimize the mask fit. However, even the best tuned masks include a small amount of contaminating flux at the expense of better capturing the HDO and $H_2{}^{18}O$ flux. HDO 241 GHz has the largest amount of contamination from its neighboring COM line, while $H_2{}^{18}O$ also has some contamination. We show the channel maps of the HDO and $H_2{}^{18}O$ emission with the Keplerian masks overlaid in Extended Data Figures 1 and 2. The Keplerian masks for the contaminating lines are also drawn to show the expected velocities and location of the contaminating emission that overlap with the HDO and $H_2{}^{18}O$ masks.

The Keplerian mask parameters used for each line are provided in Extended Data Table 2; we used consistent parameters between the Keplerian masks for the water lines and other COMs, different parameters were only necessary when the radial extent of emission was different or there were multiple hyperfine components to the transition, as in the case of $C^{17}O$. The exact same Keplerian mask parameters are used for the two HDO lines and the $H_2{}^{18}O$ line for consistency in the analysis.

We then make use of these masks to extract moment maps of the emission and construct radial intensity profiles of the HDO and $H_2{}^{18}O$ emission, using the *bettermoments* package [38, 39]. In addition to the Keplerian masks, we also apply velocity range limits on the moment map calculations to omit unavoidable contaminating flux from neighboring lines. As such, the 225 GHz HDO integrated intensity map includes velocities between 0.05 and 8.2 km s^{-1} and the 241 GHz HDO and $H_2{}^{18}O$ maps include velocities between 1.25 and 8.2 km s^{-1}. Comparing with the HDO 225 GHz line, we find that the more limited ranges for HDO at 241 GHz and $H_2{}^{18}O$ would only omit $\sim$2% of the total line flux. The integrated intensity map for HDO at 241 GHz is shown in Extended Data Figure 3.

The measured line fluxes within the Keplerian masks for HDO at 225 and 241 GHz to be 0.554$\pm$0.007 and 0.68$\pm$0.007 Jy km s^{-1}, respectively. Then the $H_2{}^{18}O$ line flux was 0.12$\pm$0.009 Jy km s^{-1}. The values for HDO 241 GHz and $H_2{}^{18}O$ are larger than they should be because flux from contaminating spectral lines is present in overlapping velocity channels and falls within the Keplerian masks. If we only integrate the line flux in the velocity range from 5.05 to 7.05 km s^{-1}, where contamination is minimal, we can scale to account for the missing flux by using the HDO 225 GHz line (ratio of the flux between 5.05 to 7.05 km s^{-1} to the total line flux, 0.37$\pm$0.008). We measure a scaled HDO 241 GHz line flux of 0.535$\pm$0.016 Jy km s^{-1} and a scaled $H_2{}^{18}O$ line flux of 0.093$\pm$0.014 Jy km s^{-1}. The scaled HDO 225 GHz line flux is identical to the measurement from the full Keplerian mask value by definition. The line fluxes from the Keplerian masks in the full and 5.05 to 7.05 km s^{-1} velocity ranges (scaled and unscaled) are provided in Extended Data Table 4.

We note that there is a small amount of contamination to the HDO 241 GHz line flux within the 5.05 to 7.05 km s^{-1} velocity range. We correct for the estimated contamination to the HDO 241 GHz line flux in this velocity range by subtracting the estimated contamination, which is 2.3% of the total

CH_3CHO line flux (0.32 Jy km s^{-1} estimated from spectral extraction, see Section 1.4.3). The 5.05 to 7.05 km s^{-1} spectral range for HDO 241 GHz corresponds to 7.33 to 9.33 km s^{-1} from line center for CH_3CHO. We then use the ratio of the total HDO 225 GHz line flux between 7.33 to 9.33 km s^{-1} to the total HDO 225 GHz line flux to estimate that HDO at 241 GHz is contaminated by ∼2.3% of the total CH_3CHO line flux. This method of removing the estimated line flux only works because between 5.05 to 7.05 km s^{-1} the CH_3CHO Keplerian mask is wholly within the HDO 241 GHz Keplerian mask.

The uncertainties on the line fluxes are statistical only and do not include the estimated 5% absolute flux calibration uncertainty.

1.4.2 Moment 0 Extraction

While the nearby COM spectral lines to the two HDO and $H_2{}^{18}O$ lines preclude a standard moment 0 map from accurately measuring the line fluxes, we can make use of a standard moment 0 map within the limited velocity range of 5.05 to 7.05 km s^{-1}. This enables us to measure both the emission morphology and the significance of the line emission for the HDO and $H_2{}^{18}O$ lines without any potential bias caused by the pixel selections of the Keplerian masks. We show the moment 0 image computed between 5.05 to 7.05 km s^{-1} in Extended Data Figure 3 and overlay the contours of the $H_2{}^{18}O$ emission on the HDO emission to demonstrate the consistency of their emission morphologies.

We also measure the line fluxes directly from these moment 0 maps within a circle having a 0.″4 radius, centered on the continuum source. We measure line fluxes of 0.244±0.007, 0.233±0.008, and 0.052±0.008 for HDO 225 GHz, HDO 241 GHz, and $H_2{}^{18}O$, respectively. The HDO 241 GHz line flux is also corrected for the same amount of contamination from CH_3CHO line flux between 5.05 to 7.05 km s^{-1} as we did when the flux was measured within a Keplerian mask in Section 1.4.1. The line fluxes are also reported in Extended Data Table 4. We do notice that the line fluxes from the standard moment 0 extraction are systematically larger than those from the Keplerian masks in the same velocity range. The ratio of the Keplerian mask measured line fluxes between 5.05 and 7.05 km s^{-1} to those from the moment 0 measurements are 0.84±0.03, 0.88±0.03, and 0.65±0.14 for HDO 225 GHz, HDO 241 GHz, and $H_2{}^{18}O$, respectively. This small discrepancy could result from the Keplerian mask excluding some line flux, but as we show later this does not lead to a significant difference in the measurement of the column densities of HDO and $H_2{}^{18}O$ nor the HDO/H_2O ratio. Moreover, the scaled line fluxes from the moment 0 analysis are consistent within the 1σ uncertainties of the line fluxes from spectral extraction (Section 1.4.3).

1.4.3 Spectral Extraction

In addition to the analysis of the data cubes, we also perform an analysis of the disk-averaged spectra. We extract the spectra around the HDO, $H_2{}^{18}O$, and methanol transitions within a 0.″4 radius circle centered on the continuum emission peak. The input data cubes are first converted from Jy $beam^{-1}$ to

Jy pix^{-1} and then all emission contained within the 0.″4 radius of the protostar position is summed, per channel, to create a one dimensional spectrum. The spectra around the HDO and $H_2{}^{18}O$ lines are shown in Extended Data Figure 4.

We also made use of spectral stacking, which removes the Keplerian kinematic pattern from the data and aligns the emitting components to be at the same velocity using the *spectral-cube* package [40, 41]. This method boosts the S/N of the spectral lines and makes the features sharper by lowering their velocity widths because of the removal of the double-peaked line shape that is associated with Keplerian rotation. The spectrally-stacked data make contaminating line features easier to identify and associate with the rest frequencies of molecular species. However, we do not perform measurements with the spectrally-stacked data because a forward model using the spectral template is expected to be more reliable. Moreover, the spectral stacking can impact the line profiles in unexpected ways if not all emission lines come from the same emission layers within the disk or the midplane. Therefore, it is advantageous to use a spectral template to forward model the raw spectra. The stacked spectral data are presented in Extended Data Figure 4 and clearly show that $H_2{}^{18}O$ is indeed detected with a peak at its expected frequency.

1.4.4 Spectral Fitting

We constructed two different template spectra to disentangle the HDO and $H_2{}^{18}O$ from the contaminating lines. First, because the integrated intensity maps for methanol, HDO, and $H_2{}^{18}O$ reveal that these molecules all have very similar spatial and velocity distributions, we used the isolated methanol lines that we detect in another spectral window as a spectral template for HDO, $H_2{}^{18}O$, and other COM lines in the disk. Second, we constructed a toy Keplerian disk model with a central protostar mass of 1.3 $M_\odot$[6] using the Line Modeling Engine (LIME) [42] radiative transfer code to simulate the expected line profile of an optically thin molecule that is present in the disk between a radius of 20 and 85 au. The model also excludes dust emission to make as ideal a spectrum as possible.

To construct the template spectrum using the methanol lines, we first extracted the 5 isolated methanol lines in our spectral window that targeted methanol at high spectral resolution (Extended Data Table 1), using the same aperture radius (0.″4) used to extract the other spectra. We then baseline subtracted the individual spectra to take out any slope in the spectral baseline. We next normalized each spectrum to have a maximum value of 1.0. Following normalization, we upsampled the spectral resolution of these lines by a factor of 6 and put all the individual methanol spectra on the same frequency axis. The spectra were averaged together to make a higher S/N template spectrum. We again baseline subtracted the new template spectrum to take out an residual slope in the spectral baselines. Finally, we mirrored the spectrum and averaged the mirror with itself to create a symmetric spectral profile. The

mirroring creates a more idealized line profile for modeling emission lines other than methanol that may not have the exact same line shape.

To extract the 1 dimensional spectrum from the LIME model, we use the same routines that we used to extract the spectra from the real data cubes, and the 0.″4 extraction radius encompasses all the emission in the model. We also mirror this spectrum to smooth out any asymmetries that remain from the model gridding and noise in the radiative transfer calculations. The LIME and methanol template spectra are shown in Extended Data Figure 5. The wings of the template lines agree well, and the primary difference is in the central portion of the line, and to a lesser extent the location of the symmetric peaks. This difference is due to the high opacity of the methanol lines, which causes the center of their line profiles to appear more filled-in relative to the peaks at higher and lower frequencies. These template spectra enable us to deblend the HDO and $H_2{}^{18}O$ lines from the COM lines without using the spectrally-stacked data. Both spectral templates are resampled to the lower spectral resolution of the data for fitting.

The HDO lines were all brighter than the nearby contaminating COM lines, and each HDO line was blended with ∼2 COM lines. Generally a single line was the primary contaminating feature and there was tentative contamination from a second COM line. Then $H_2{}^{18}O$ had contamination primarily from one nearby COM line, but two other lines of the same species are also nearby. We list the most likely contaminating COM lines in Extended Data Table 3. The plausibility of the contaminating features relied on the positive identification of the species toward V883 Ori from previous work [15] and that the feature could be present with a reasonable column density (10^{14}-10^{16} cm^{-2}) and a temperature of 200-300 K, as simulated with the eXtended CASA Line Analysis Software Suite (XCLASS) [43]. Similar to previous work, we find that $H_2{}^{18}O$ has contamination from CH_3OCH_3, HDO 225 GHz has contamination from CH_3OCHO [21, 22], but we also find that HDO at 225 GHz could be contaminated by $^{13}CH_3CHO$ (an acetalaldehyde isotopologue). Then, HDO at 241 GHz was found to be most likely contaminated by CH_3CHO, with a possible second, weaker contaminating feature from $(CH_3)_2CO$ (acetone).

With the frequencies of the contaminating lines identified, and the well-constrained velocity of the source (4.25 km s^{-1}) determined from the high-spectral resolution methanol emission detected in our data set, we are able to model the spectral features of HDO and $H_2{}^{18}O$ and their surrounding lines with a linear addition of the scaled template spectra. We provided the rest frequencies for each line and used the *scipy* function *minimize* to find the best fitting multiplicative factors to fit the spectra using scaled spectral templates; rest frequencies of the spectral features were kept fixed. The results of the spectral fitting are shown in Extended Data Figure 4.

We decided to adopt the optically-thin spectral template for our fiducial model because it qualitatively fits the HDO spectra better than the methanol model. However, the subtle differences in the line fluxes whether we use the optically-thin model, the methanol model, or the optically-thin model for HDO

and $H_2{}^{18}O$ and the methanol model for COMs does impact the excitation temperature, and hence the line column densities and HDO/H_2O ratios. However, the HDO/H_2O ratios are all consistent within their 1σ uncertainties, so the choice of model does not significantly impact the results as a whole.

The line fluxes were measured from the spectrum with the contaminating COM lines subtracted and uncertainties are derived from the RMS of the residual spectrum with all fitted lines removed. This approach takes into account any uncertainties associated with imperfect fitting of the contaminating lines. We also tested Markov-Chain Monte Carlo methods to fit the spectra, but the results did not differ from the maximum likelihood fit using *scipy's minimize* function. However, to validate our assumption of a fixed velocity and not allow the source velocity to be optimized, we randomly sampled velocities within 5% of 4.25 km s^{-1} and determined if the width of the distribution of fitted line flux densities was smaller or larger than the statistical uncertainty from the RMS of the residuals. For all the water lines, the statistical uncertainty was smaller than the error in flux that could result from an imperfect system velocity. The line fluxes derived from the spectral template models are given in Extended Data Table 4.

The measurements of the line fluxes for all spectral template models are not entirely in agreement between the spectral fitting methods, Keplerian mask extraction methods, and scaled moment 0 methods. Some differences can be explained by contamination of the HDO 241 GHz line in particular, but the largest differences are for the HDO 225 GHz line flux from the Keplerian mask and the scaled moment 0 line flux from the 5.05 to 7.05 km s^{-1} moment 0 map. But, most flux differences are within 3σ, and the with HDO 241 GHz and $H_2{}^{18}O$ being consistent within 2σ. Some difference can be expected for multiple reasons. First, we integrate the spectra over the same circular aperture in all channels, while the Keplerian mask has more limited spatial extent because it only covers the portion of the disk expected to be emitting at a particular velocity. However, the projected outer extent of the Keplerian masks is comparable to 0.″4 spectral extraction radius. Second, the masks are also more limited in their spectral extents to avoid too much contamination from other lines, particularly for HDO at 241 GHz and $H_2{}^{18}O$. Third, some true line emission can extend beyond the Keplerian mask at a given velocity channel and this would be specifically excluded from the Keplerian mask line flux, but included in the integrated spectrum. The most easily quantified difference is the difference in spectral range of the Keplerian mask, which results in just a 2% flux difference. The impact of these differences on the resultant column densities are explored further in section 1.4.6.

1.4.5 Measuring Column Densities

We measure the column densities of HDO and $H_2{}^{18}O$ following standard methods under the assumption that the lines are optically thin and in local thermodynamic equilibrium (LTE) [44]. The spectral line parameters and partition functions were taken from the NASA JPL database [45]. We first measure

the line integrated intensities in units of Jy km s^{-1}, which we then convert to temperature units via

$$\int T_B \, dv = \frac{c^2}{2\nu^2 k_B \Omega} \int F_\nu \, dv, \tag{1}$$

where k_B is the Boltzmann constant, $\Omega = \pi R^2$, and R is the 0.″4 aperture radius (converted to radians) used for extracting the spectra. For the radial profiles, they are extracted from the data cubes in K km s^{-1} using the *bettermoments* package [38, 39].

The column densities of the upper energy level are determined from the equation

$$N_u = \frac{8\pi k_B \nu_u^2}{hc^3 A_{ul}} \int T_B \, dv \tag{2}$$

where h is Planck's constant, and A_{ul} is the Einstein A coefficient for the transition. An estimate of the excitation temperature is then needed to determine total column densities, which we obtain from the ratio of column densities in the HDO 225 GHz and 241 GHz lines via

$$T_{ex} = \frac{E_{u,225GHz} - E_{u,241GHz}}{ln\left(\frac{N_{u,225GHz}}{N_{u,241GHZ}} \frac{g_{u,241GHz}}{g_{u,225GHz}}\right)} \tag{3}$$

where E_u is the upper level energy of the two HDO transitions and g_u is the statistical weight for each transition. Then the total column density for each transition is given by

$$N = \frac{N_u}{g_u} \, Q_{rot}(T_{ex}) \, e^{\frac{E_u}{T_{ex}}} \tag{4}$$

where $Q_{rot}(T_{ex})$ is the partition function. We use the tabulated partition functions from the JPL database as a function of temperature for HDO and $H_2{}^{18}O$, and for T_{ex} values in between the tabulated temperatures we interpolate. Also, we use the full partition function for $H_2{}^{18}O$ which includes both the ortho and para states, implicitly correcting for the ortho to para ratio (OPR) of $H_2{}^{18}O$. The calculated values for the interpolated partition functions are listed in Extended Data Table 4. The OPR for $H_2{}^{18}O$ is assumed to be 3, substantial differences from this amount are not expected. The comet 67P was found to have an OPR of 2.94±0.06 [46], which is consistent with the laboratory work finding that evaporating ices have an OPR of 3 [47]. We convert the $H_2{}^{18}O$ column density to an H_2O column density by multiplying by the $^{16}O/^{18}O$ ratio of 560±25 [48]. However, we do know that the $^{16}O/^{18}O$ in 67P for H_2O is 445±35 [49]. Therefore, it is possible that the actual H_2O column densities in V883 Ori are lower, which would further elevate the HDO/H_2O ratio.

The uncertainties in the column densities and ratios are derived from standard error propagation. The uncertainty on the HDO column densities includes the random measurement error from the noise in each channel, the ∼5% absolute flux density calibration uncertainty (only included once in the average

HDO column density since both lines are observed simultaneously), and the uncertainty in the excitation temperature. The $H_2{}^{18}O$ also includes the additional uncertainty on the ratio of $^{16}O/^{18}O$ (neglecting the possibility of a large systematic uncertainty). These uncertainties are all propagated into the HDO/H_2O ratio such that the uncertainties on our derived ratio include all the known uncertainties and better reflect the absolute accuracy of the measurement versus only including statistical measurement uncertainties. Finally, we did not make a correction for additional dust attenuation of the 225 and 241 GHz HDO lines relative to $H_2{}^{18}O$ at 203 GHz when calculating the HDO/H_2O ratio. This correction would have a radial dependence and would depend on the adopted power-law dust opacity dependence with frequency. The application of such a correction would only result in a *higher* HDO column density and a higher HDO/H_2O ratio since dust attenuation is larger at higher frequencies.

We further note that the excitation temperature derived is not expected to be very accurate because of the small range of upper level energies sampled by the HDO lines (95 and 167 K), but the HDO/H_2O ratio only varies by a factor of $\sim$2 for temperatures between 75 K to 225 K, so the precision of the excitation temperature is not extremely important.

The assumption of LTE is appropriate for the V883 Ori disk. The critical densities of the HDO 225 GHz, 241 GHz, and $H_2{}^{18}O$ 203 GHz are 9.72×10^5 cm^{-3}, 1.06×10^6 cm^{-3}, and 3.79×10^5 cm^{-3}, respectively, using the collision coefficients for a temperature of $\sim$200 K from the Leiden Atomic and Molecular Database (coefficients for para-H_2O are used for para-$H_2{}^{18}O$) [50, 51]. These critical densities are satisfied even for protostars where the origin of the emission is likely to have contributions from the envelope outside the disk. Moreover, previous analyses have examined the difference between LTE and radiative transfer models that take into account non-LTE effects [21, 22]. Those studies find that the HDO/H_2O ratios derived from non-LTE modeling are consistent with the LTE calculations or differ by only factors of 3 to 4. Also, they often indicate even higher HDO/H_2O ratios and are thus not regarded as being more accurate. Finally, a simple estimate of the disk density in the upper layers at a height of 50 au and a radius of 80 au we find that the density would be $\sim7.4\times10^6$ cm^{-3}. All other emission would be from lower layers at higher density and also fulfilling the conditions for LTE. We estimated the disk density by assuming parameters typical for an irradiated disk using a parameterized surface and vertical density profile [52]

$$\rho(r,z) = \frac{\Sigma(r)}{\sqrt{2\pi}H} exp\left(-\frac{z^2}{2H(r)^2}\right). \tag{5}$$

where $\Sigma(r)$ is

$$\Sigma(r) = \Sigma_0 \left(\frac{r}{10\ au}\right)^{-1} \tag{6}$$

and Σ_0=100 g cm^{-2}, as is typical for a ∼0.01 M$_\odot$ proto-planetary disk [17], chosen as a conservative lower limit. $H(r)$ for the gas disk is parameterized as

$$H = 1.0\ au \left(\frac{r}{10au}\right)^{1.25} \quad (7)$$

which is typical for an irradiated disk.

1.4.6 HDO/H_2O Results From Keplerian Mask and Moment 0 Line Fluxes

We noted earlier that the line fluxes extracted using a Keplerian mask and integrated intensity maps from 5.05 to 7.05 km s^{-1} differed from those derived from the spectrum and it is worthwhile to examine how line flux extraction using the Keplerian mask would affect our results. Note that we correct for the 2% reductions to the HDO 241 GHz and $H_2{}^{18}O$ line fluxes due to the smaller channel ranges used relative to HDO 225 GHz in their line flux measurements in the calculations that follow. The values for the line fluxes used to calculate the column densities mentioned in the text below are also provided in Extended Data Table 4, in addition to the HDO/H_2O ratios.

We examined line flux measurements that used the full Keplerian mask, which includes some unavoidable contamination from COMs in the 241 GHz and $H_2{}^{18}O$ channel maps. The contamination is difficult to avoid when using an identical Keplerian mask to the HDO 225 GHz line. Because of the contaminated line fluxes to the HDO 241 GHz line, the lower excitation HDO transition (Extended Data Table 3), the excitation temperature is found to be lowest for the full Keplerian mask measurement at 112±3 K. Then the HDO and $H_2{}^{18}O$ column densities are measured to be (5.07 ± 0.26)×10^{15} cm^{-2} and (4.75 ± 0.44)×10^{15} cm^{-2}, respectively. These measurements are both lower than those from the spectral extraction, but are consistent at the 1.4 and 0.5σ levels, respectively. The inferred H_2O column density is (2.66 ± 0.28)×10^{18} cm^{-2}, which is corrected for the ^{16}O to ^{18}O ratio and the ortho to para ratio of 3. The HDO and H_2O column densities then yield a HDO/H_2O ratio of (1.91 ± 0.22)×10^{-3}, which is consistent with the value from spectral extraction within the uncertainties.

Because of the known significant contamination of HDO 241 GHz and $H_2{}^{18}O$ using the same Keplerian mask as HDO 225 GHz, without further optimization, we also examined the measurements obtained by integrating the flux density within a mostly contamination free region of the data cube (5.05 to 7.05 km s^{-1}) and scaling the line flux from that spectral range to the expected flux from the full spectral range using the ratio of HDO 225 GHz flux integrated within a Keplerian mask to the HDO 225 GHz flux present between 5.05 to 7.05 km s^{-1} (0.37±0.008), also within a Keplerian mask. The HDO/H_2O ratio remains unchanged whether we only compare line fluxes between 5.05 to 7.05 km s^{-1} or scale to the expected full line flux, but to compare the column densities consistently, we need to make use of the scaled line fluxes.

The HDO, $H_2{}^{18}O$, and inferred H_2O column densities derived from scaled line fluxes measured within a Keplerian mask from 5.05 to 7.05 km s^{-1} are $(5.36 \pm 0.35)\times10^{15}$ cm^{-2}, $(3.76 \pm 0.58)\times10^{15}$ cm^{-2}, $(2.11 \pm 0.34)\times10^{18}$ cm^{-2}, and respectively, using the calculated excitation temperature of 162±11 K. These measurements are both lower than those from the spectral extraction, but are consistent at the 1.1 and 1σ levels, respectively. The HDO and H_2O column densities then yield a HDO/H_2O ratio of $(2.54 \pm 0.44)\times10^{-3}$, which is consistent within the uncertainties with the value from spectral extraction.

Then, if we instead derive the column densities using the line fluxes measured from the standard moment 0 image computed between 5.05 to 7.05 km s^{-1}, we measure HDO, $H_2{}^{18}O$, and inferred H_2O column densities of $(6.78 \pm 0.62)\times10^{15}$ cm^{-2}, $(5.92 \pm 1.00)\times10^{15}$ cm^{-2}, $(3.31 \pm 0.59)\times10^{18}$ cm^{-2}, and respectively, using the calculated excitation temperature of 182±19 K. These values are consistent with the values from spectral extraction within the uncertainties. The HDO and H_2O column densities then yield a HDO/H_2O ratio of $(2.05 \pm 0.41)\times10^{-3}$, which is consistent within the uncertainties with the value from spectral extraction.

The high degree of consistency of the between the methods of spectral extraction, standard Keplerian mask, Keplerian mask between 5.05 and 7.05 km s^{-1}, and a standard moment 0 between 5.05 and 7.05 km s^{-1} indicates that multiple methods arrive at compatible measurements for the HDO and $H_2{}^{18}O$ column densities and consistent measurements of the HDO/H_2O ratio. While the line contamination present in the case of the standard Keplerian mask of the full velocity range is not ideal, it also does not significantly alter the main result. Thus, we conclude that the method of line flux measurement does not significantly affect our results on the column densities and HDO/H_2O ratio measured. The Keplerian mask and standard moment 0 measurements do, however, tend to have lower uncertainties because they make use of measurements over smaller ranges of velocity and/or a smaller number of pixels (via the mask) which reduces the noise that is added from the summation of multiple channels. We still favor the spectral analysis method since this makes use of the full spectral range of the data rather than subsets of the full dataset.

1.5 Birth Environment of V883 Ori Relative to the Sun and Other Protostars

V883 Ori is compared with Class 0 protostars, comets, and water in Earth's oceans in Figure 4 attempting to determine if there is an evolutionary sequence in the HDO/H_2O ratios. However, we already know that V883 Ori has formed in a somewhat different environment compared to the Sun/Solar System and other Class 0 protostars. V883 Ori is forming within the Orion A giant molecular cloud and is ∼10 pc from the main cluster/nebula and the nearest protostar is ∼0.4 pc away, both measurements are in projected distance, thus it is relatively isolated within Orion. In contrast, the Class 0 protostars with measured HDO/H_2O ratios come from a mix of isolated and protostars within small clusters [22], and the isolated Class 0 protostars have systematically higher

HDO/H_2O ratios. V883 Ori's HDO/H_2O ratio is most similar to the isolated Class 0 protostars. This may make sense because it is relatively isolated itself, but the isolated protostars are forming in truly isolated cores and are not part of a larger molecular cloud, unlike V883 Ori. It is still unknown what causes the higher HDO/H_2O ratios for isolated systems, but it remains to be seen if the difference between isolated and clustered protostars remains with larger samples.

The Sun and Solar System were most likely formed in a cluster within a giant molecular cloud, which could have been similar to Orion [53, 54]. However, the dynamical constraints that are available for the evolution of the Solar System point to its formation environment being closer to, or within the main cluster [55]. Thus, V883 Ori is not forming in completely analogous conditions relative to the early Solar System. Nonetheless, it is still extremely relevant to compare the measurements for V883 Ori to comets within the Solar System and Earth given that they represent the only available measurements of more-evolved bodies. Furthermore, if water is inherited relatively unchanged from the cold molecular cloud phase, the fact that both the Sun/Solar System and V883 Ori formed within giant molecular clouds, suggests that it is reasonable to compare the HDO/H_2O ratios of these systems.

1.6 Measurements of D/H Ratios from the Literature

To create Figure 4, we collected various published measurements for protostars and comets from the literature. We have assembled these measurements in Extended Data Table 5 for reference.

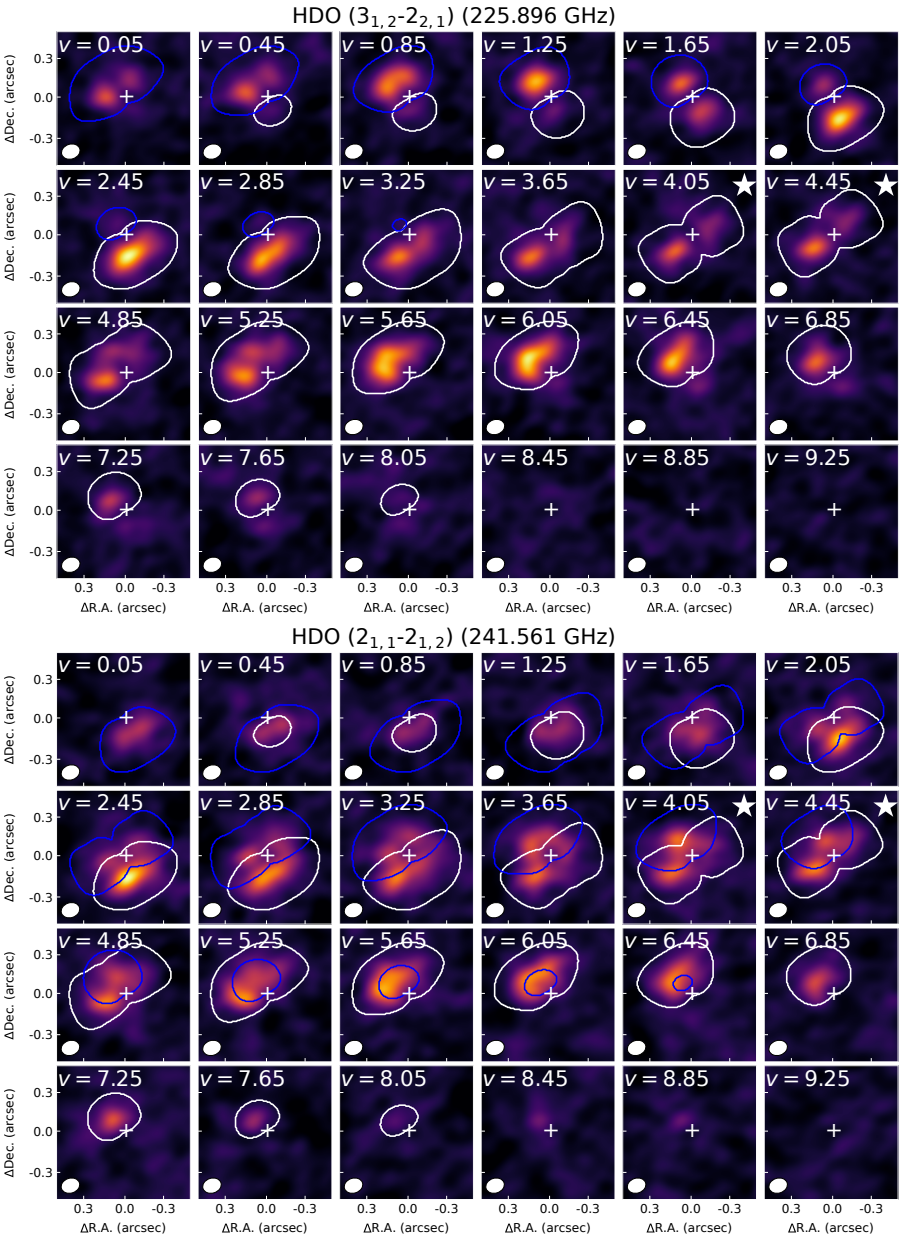

Extended Data Figure 1 Channel maps of HDO 225 and 241 GHz emission. The data are shown by the color scale, the Keplerian mask is drawn as the heavy white line, and the mask corresponding to the blueshifted CH_3OCHO line (Extended Data Figure 4) is drawn as the heavy blue line for HDO 225 GHz and CH_3CHO for HDO 241 GHz. The continuum peak/protostar position is marked by the white cross. The channels nearest the velocity of V883 Ori (4.25 km s^{-1}) are marked with a star in the upper right corner. The synthesized beam is also drawn in the lower left corner of each panel.

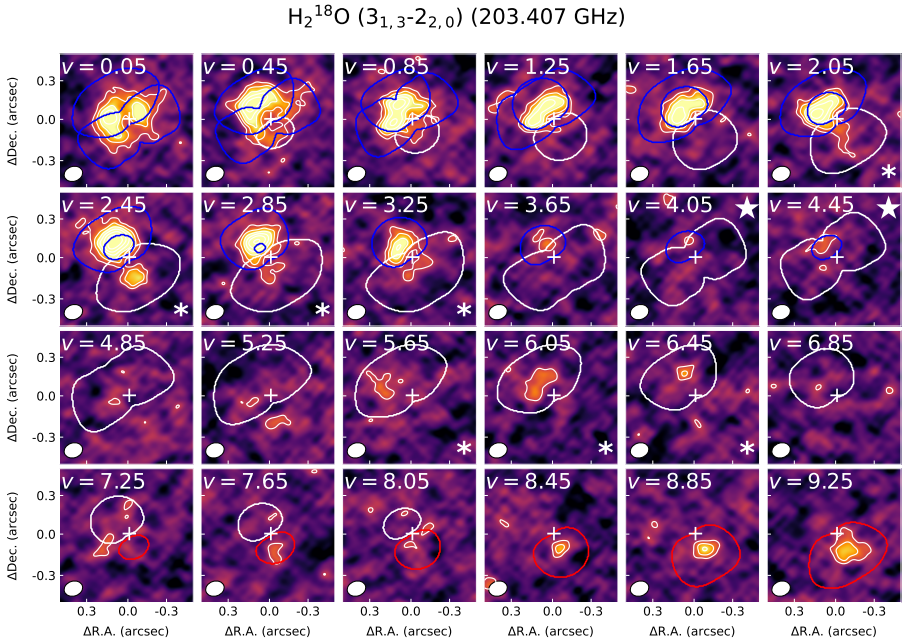

Extended Data Figure 2 Channel maps of $H_2{}^{18}O$ 203 GHz emission. The data are shown by the color scale, the Keplerian mask for $H_2{}^{18}O$ is drawn as the heavy white line, and the masks corresponding to the two blueshifted and one redshifted CH_3OCH_3 lines (Extended Data Figure 4) are drawn as the heavy blue and red lines, respectively. The continuum peak/protostar position is marked by the white cross and the channels nearest the velocity of V883 Ori (4.25 km s^{-1}) are marked with a star in the upper right corner. Despite the faintness of the $H_2{}^{18}O$ line and its location between nearby COM lines, the detection of $H_2{}^{18}O$ is unambiguous given that its emission is detected in the expected channels for the given protostar mass. The channels with $>3\sigma$ detections within the Keplerian masks are marked with asterisks in the lower right corner. The synthesized beam is drawn in the lower left corner of each panel.

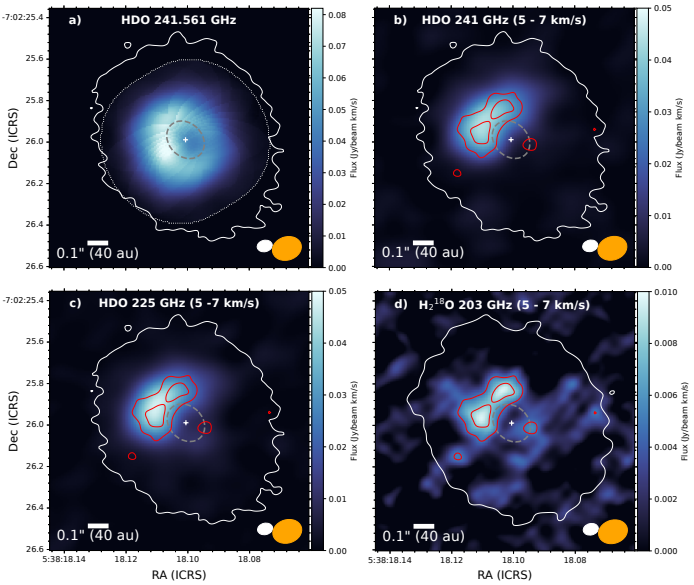

Extended Data Figure 3 Integrated intensity images of HDO and $H_2{}^{18}O$. The HDO 241 GHz integrated intensity map created using a Keplerian mask identical to the HDO 225 GHz and $H_2{}^{18}O$ lines is shown in panel a), the HDO 241 GHz integrated intensity image between 5.05 and 7.05 km s^{-1} is shown in panel b), the HDO 225 GHz integrated intensity image using the same velocity range is shown in panel c), and the $H_2{}^{18}O$ integrated intensity image from the same velocity range is shown in panel d). The contours shown in panels b, c, and d are from the $H_2{}^{18}O$ image and show the intensity levels 3 and 5 times the noise (s.d.), where 1 s.d. is 0.00158 Jy beam^{-1} km s^{-1}, and the integrated intensity images in these panels were computed without the use of masks or any other clipping. The 5.05 to 7.05 km s^{-1} velocity range had minimal contamination from other lines for HDO and $H_2{}^{18}O$ and effectively demonstrates the significance of the $H_2{}^{18}O$ detection. The extent of the continuum emission from the disk is denoted by the white contour and the position of the protostar is marked with the white cross. The HDO 241 GHz line shows very similar structure to the HDO 225 GHz line that is shown in Figure 2 in the main text, and the dotted line in panel a) shows the region over which the integrated intensity image was computed using the Keplerian mask. The depression in the center of the line emission in panel a) is the result of optically thick continuum absorbing the line emission in the inner $\sim$0.″1 (40 au). The extent of this optically thick region is denoted with the thick gray line in the center of each image. The ellipses in the lower right corner denote the resolution of the line observation (orange, $\sim$0.″1) and the continuum data (white, $\sim$0.″08).

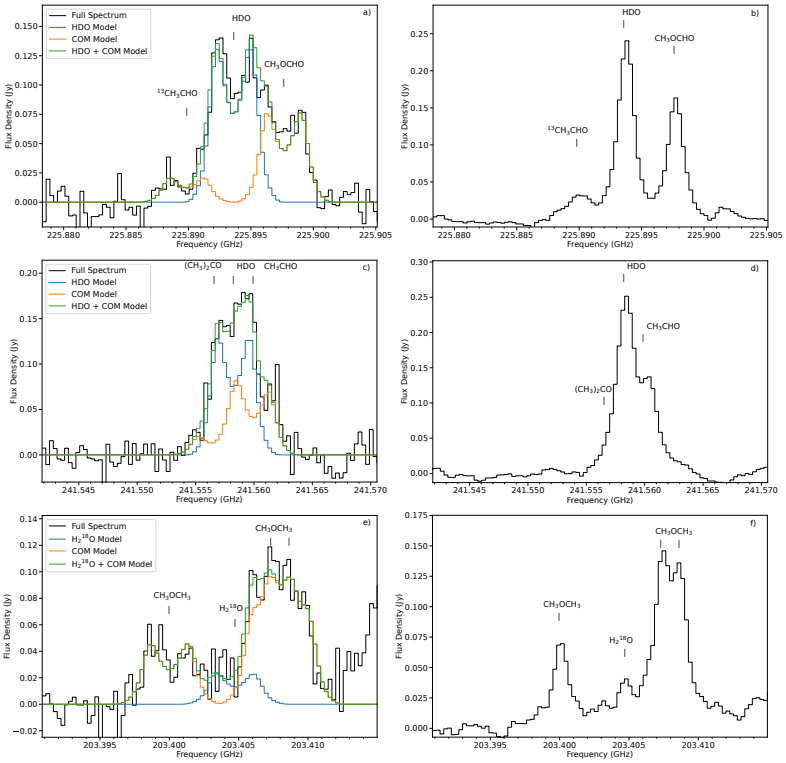

Extended Data Figure 4 Integrated spectra of V883 Ori centered on the HDO 225 GHz, HDO 241 GHz, and $H_2{}^{18}O$ 203 GHz lines. The panels a), c), and e) show the spectra as observed (disk rotation causes all spectral lines to have a double-peaked line profile), while the panels b), d), and f) show the stacked spectra [40, 41] with the Keplerian rotation profile removed. The root mean squared (RMS) noise of the HDO 225 GHz, HDO 241 GHz, and $H_2{}^{18}O$ are 0.016, 0.017, and 0.011 Jy, respectively. The HDO lines are the brightest features around their center frequencies, but both have contaminating emission from COM species nearby. The $H_2{}^{18}O$ line is faint relative to its surrounding features but is still clearly detected. We are able to model the spectral profiles for HDO and $H_2{}^{18}O$ and the contaminating lines to measure their line fluxes using an optically-thin synthetic spectral model for a disk. (Extended Data Figure 5). In panels a), c), and e), the observed spectrum is drawn as the black line, the model of the contaminating lines is drawn as an orange line, the model HDO and $H_2{}^{18}O$ lines are drawn as blue lines, and the total model of contaminating lines with HDO and $H_2{}^{18}O$ is drawn as a green line. The rise seen toward higher frequencies on the $H_2{}^{18}O$ spectrum (panel e) is another CH_3OCH_3 line that peaks outside the shown region. The spectra are plotted at their observed frequencies and are not corrected for the system local standard of rest (LSR) velocity of $\sim$4.25 km s^{-1}.

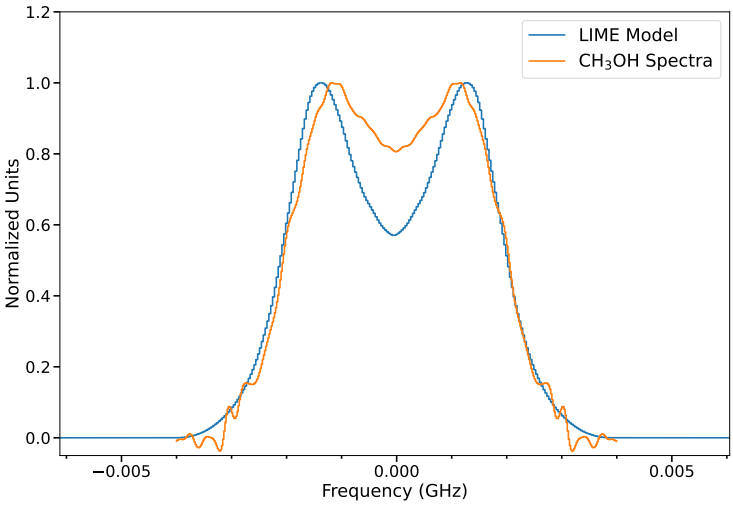

Extended Data Figure 5 Plot of template spectra derived from the LIME radiative transfer model and from the observed isolated methanol lines. The main difference between the templates is at the center of the line profile where the methanol line has a much more shallow dip due to line optical depth, while the optically thin LIME model has a much deeper dip at the center and sharper peaks.

Extended Data Table 1. Spectral Setup

Line	Rest Frequency (GHz)	Band Width (MHz)	Spectral Resolution (KHz, km s^{-1})	Beam ($''$)
Band 5 Data				
$H_2^{18}O$ 3(1,3)- 2(2,0)	203.40752	234.375	122.070, 0.18	0.142×0.112
CH_3CN[a]	202.351612	234.375	122.070, 0.18	0.143×0.113
Continuum	190.5	1875	1129, 1.777	0.150×0.122
Continuum	188.7	1875	1129, 1.794	0.151×0.121
Band 6 Data				
H_2CO 3(1,2)-2(1,1)	225.697775	58.594	122.070, 0.162	0.105×0.083
CH_3OD 5(0,5)-4(0,4) A	226.538674	58.594	122.070, 0.162	0.105×0.083
$C^{17}O$ J=2-1	224.714373	58.594	122.070, 0.162	0.106×0.083
HDO 3(1,2)-2(2,1)	225.89672	58.594	122.070, 0.162	0.104×0.082
CN[a]	226.6595584	117.188	141.113, 0.187	0.102×0.081
CN[a]	226.87478	117.188	141.113, 0.186	0.102×0.081
Continuum	240.5	1875	1129, 1.407	0.099×0.078
HDO 2(1,1)-2(1,2)	241.56155	117.188	122.070, 0.152	0.098×0.077
CH_3OH[a]	241.83165	117.188	122.070, 0.151	0.098×0.078
CH_3OH[b] 5(4)- - 4(4)-	241.806524	”	”	”
CH_3OH[b] 5(-4) - 4(-4) E2	241.813255	”	”	”
CH_3OH[b] 5(-3) - 4(-3) E2	241.852299	”	”	”
CH_3OH[b] 5(1) - 4(1) E1	241.879025	”	”	”
CH_3OH[b] 5(2)+ - 4(2)+	241.887674	”	”	”

Note. — While spectral windows are identified as targeting a particular line or continuum, they also generally contain spectral features from other molecules.

[a]Several features of this molecule are contained within the spectral window.

[b]Methanol lines that were isolated enough to use for creation of a template spectrum.

Extended Data Table 2. Keplerian Mask Parameters

Datacube	Line	V_{sys} (km s^{-1})	Smoothing (Frac. Beam)	R_{max} (arcsec)	Z/R	ΔV (km s^{-1})
HDO 225 GHz						
	HDO 3(1,2)-2(2,1)	4.25	1.25	0.3	0.4	0.35
	CH_3OCHO 225.90074 GHz	-1.09[b]	1.25	0.3	0.4	0.35
HDO 241 GHz						
	HDO 2(1,1)-2(1,2)	4.25	0.5	0.3	0.2	0.35
	CH_3CHO 241.5632277 GHz	2.17[b]	0.5	0.3	0.2	0.35
H_2CO						
	H_2CO 3(1,2)-2(1,1)	4.25	1.75	0.9	0.2	1.0
$C^{17}O$						
	$C^{17}O$ (J=2-1)[a]	3.7	1.25	0.85	0.2	1.2
	$C^{17}O$ (J=2-1)[a]	4.6	1.25	0.85	0.2	1.2
CH_3OH						
	241.887674 GHz	-50.4[b]	1.75	0.4	0.4	0.35
	241.879025 GHz	-39.7[b]	1.75	0.4	0.4	0.35
	241.852299 GHz	-6.5[b]	1.75	0.4	0.4	0.35
	241.813255 GHz	41.9[b]	1.75	0.4	0.4	0.35
	241.806524 GHz	50.3[b]	1.75	0.4	0.4	0.35
$H_2^{18}O$						
	$H_2^{18}O$ 3(1,3)- 2(2,0)	4.25	1.25	0.3	0.4	0.35

Note. — All masks assumed a stellar mass of 1.285 $M_\odot$, an inclination of 38.3°, a position angle of 32°, a distance of 400 pc, and an inner radius of 0.″1. H_2CO and $C^{17}O$ both used an inner radius of 0.″05.

[a]These masks were combined to make a single mask because $C^{17}O$ ($J = 2 \rightarrow 1$) has 4 blended hyperfine components causing its emission to be spread over a wider range of channels than emission from a single spectral line.

[b]Offset velocity from the rest frequency of the cube, adopted source velocity was 4.25 km s^{-1}.

Extended Data Table 3. Spectral lines Blended with HDO and $H_2^{18}O$

Molecule	Transition	Rest Frequency (GHz)	Upper Level Energy (K)	Einstein A (log_{10} (s^{-1}))	RMS[a] (Jy)
$H_2^{18}O$					0.011
$H_2^{18}O$	3(1,3)- 2(2,0)	203.40752	203.7	-5.31770	
CH_3OCH_3	3(3, 1)- 2(2, 1) EE	203.4101126	18.1	-4.26493	
CH_3OCH_3	3(3, 0)- 2(2, 1) AE	203.4114309	18.1	-4.02956	
CH_3OCH_3	3(3, 1)- 2(2, 1) EA	203.4027779	18.1	-4.18698	
HDO 225 GHz					0.016
HDO	3(1,2)-2(2,1)	225.89672	167.6	-4.87987	
CH_3OCHO	6(6,0)- 5(5,0) E	225.90074	36.3	-4.58474	
$^{13}CH_3CHO$[b]	12(2,10) - 11(2,9) E, vt=1	225.8929484	285.7	-3.40579	
HDO 241 GHz					0.017
HDO	2(1,1)-2(1,2)	241.56155	95.2	-4.92559	
CH_3CHO	21(2,19)-20(3,18) E	241.5632277	226.4	-4.70342	
$(CH_3)_2CO$	13(10, 4)-12(9, 3) AA	241.5598869	77.7	-3.48114	

[a]RMS noise of a line-free region of the spectrum.

[b]Tentatively identified line.

Extended Data Table 4. Impact of Different Spectral Models or Line Flux

Model	Temp. (K)	Q(T)[a] (HDO, $H_2{}^{18}O$)	HDO/H_2O	HDO(225) (Jy km s^{-1})	HDO(241) (Jy km s^{-1})	$H_2{}^{18}O$ (Jy km s^{-1})
Optically-thin	199±42	80.6, 98.8	$(2.26\pm0.63)\times10^{-3}$	0.644±0.028	0.595±0.037	0.126±0.025
Methanol	210±48	86.7, 106.2	$(1.85\pm0.51)\times10^{-3}$	0.64±0.024	0.581±0.04	0.155±0.025
Both[b]	276±87	130.6, 159.8	$(1.92\pm0.49)\times10^{-3}$	0.653±0.026	0.546±0.040	0.159±0.024
Kep. Mask [c]	112±3	35.2, 43.3	$(1.91\pm0.22)\times10^{-3}$	0.554±0.007	0.680±0.007	0.111±0.009
5.05 to 7.05 km s^{-1}[d]						
Kep. Mask[e]	162±10	59.5, 73.0	$(2.54\pm0.44)\times10^{-3}$	0.205±0.004	0.206±0.004	0.034±0.005
Kep. Mask (scaled)[f]	162±10	59.5, 73.0	$(2.54\pm0.44)\times10^{-3}$	0.554±0.007	0.555±0.016	0.093±0.014
Moment 0[g]	182±19	70.7, 86.6	$(2.05\pm0.41)\times10^{-3}$	0.244±0.007	0.233±0.008	0.052±0.008
Moment 0 (scaled)[h]	182±19	70.7, 86.6	$(2.05\pm0.41)\times10^{-3}$	0.658±0.018	0.63±0.020	0.14±0.023

[a]Calculated value of the partition function at the listed temperature.

[b]The optically thin model is used for the HDO and $H_2{}^{18}O$ lines while the methanol model is used for the COM lines.

[c]Line fluxes measured straight from Keplerian masks, without fine-tuned masks to avoid contamination for $H_2{}^{18}O$ or HDO 241 GHz. As such, the HDO 241 GHz and $H_2{}^{18}O$ line fluxes are overestimated and the excitation temperature is underestimated.

[d]Measurements are based line flux measurements only within 5.05 to 7.05 km s^{-1}

[e]HDO(241) has its flux reduced by 0.007 Jy km s^{-1} to account for minor contamination from CH_3CHO in its Keplerian mask.

[f]The ratio of HDO (225) line flux from 5.05 to 7.05 km s^{-1} to its total line flux (0.37±0.008) is used to scale the HDO(241) and $H_2{}^{18}O$ line fluxes to their expected values for the full velocity range.

[g]Line fluxes are summed in a $0''.4$ radius aperture.

[h]Line fluxes are summed in a $0''.4$ radius aperture, and scaled using the ratio of HDO (225) line flux from 5.05 to 7.05 km s^{-1} to its total line flux (0.37±0.008) from the Keplerian Mask measurement.

Extended Data Table 5. D/H Measurements

Object	HDO/H_2O	Method	Reference
Earth			
Earth's Oceans	$(3.11 \pm 0.002) \times 10^{-04}$	VSMOW	[56, 57]
Oort Cloud comets			
1/P Halley	$(4.20 \pm 0.6) \times 10^{-4}$	H_2DO^+/H_3O^+	[58]
C/1996 B2 Hyatuake	$(5.80 \pm 2.0) \times 10^{-4}$	HDO/H_2O	[59]
C/1995 O1 Hale-Bopp	$(6.60 \pm 1.6) \times 10^{-4}$	HDO/H_2O	[60]
C/2007 B3 Lulin	$<1.12 \times 10^{-3}$	HDO/H_2O	[61]
8P/Tuttle	$(8.20 \pm 3.0) \times 10^{-4}$	HDO/H_2O	[62]
C/2009 P1 Garradd	$(4.12 \pm 0.44) \times 10^{-4}$	HDO/H_2O ($H_2{}^{18}O$)	[63]
C/2002 T7 LINEAR	$(5.00 \pm 1.4) \times 10^{-4}$	OD/OH (^{18}OH)	[64]
153P Ikeya-Zhang	$(5.60 \pm 0.6) \times 10^{-4}$	HDO/H_2O ($H_2{}^{18}O$)	[65]
C/2012 F6 Lemmon	$(6.50 \pm 1.6) \times 10^{-4}$	HDO/H_2O ($H_2{}^{18}O$)	[66]
C/2014 Q2 Lovejoy	$(1.40 \pm 0.4) \times 10^{-4}$	HDO/H_2O ($H_2{}^{18}O$)	[66]
Jupiter Family comets			
45P Honda-Mrkos-Pajdusakov (HMP)	$<4.00 \times 10^{-4}$	HDO/H_2O ($H_2{}^{18}O$)	[67]
103P Hartley 2	$(3.20 \pm 0.5) \times 10^{-4}$	HDO/H_2O ($H_2{}^{18}O$)	[68]
67/P Churyumov-Gerasimenko	$(1.06 \pm 0.14) \times 10^{-3}$	HDO/H_2O ($H_2{}^{18}O$)	[24, 26]
46P/Wirtanen	$(3.20 \pm 1.3) \times 10^{-4}$	HDO/H_2O ($H_2{}^{18}O$)	[69]
Flat Spectrum Disk			
V883 Ori	$(2.26 \pm 0.63) \times 10^{-3}$	HDO/H_2O ($H_2{}^{18}O$)	This work
Clustered Class 0 Protostars			
NGC1333 IRAS 4A-NW	$(5.40 \pm 1.5) \times 10^{-4}$	HDO/H_2O ($H_2{}^{18}O$)	[21]
NGC1333 IRAS 2A	$(7.40 \pm 2.1) \times 10^{-4}$	HDO/H_2O ($H_2{}^{18}O$)	[21]
NGC1333 IRAS 4B	$(5.90 \pm 2.6) \times 10^{-4}$	HDO/H_2O ($H_2{}^{18}O$)	[21]
IRAS 16293–2422	$(9.20 \pm 2.6) \times 10^{-4}$	HDO/H_2O ($H_2{}^{18}O$)	[21]
Isolated Class 0 Protostars			
BHR71 IRS	$(1.80 \pm 0.4) \times 10^{-3}$	HDO/H_2O ($H_2{}^{18}O$)	[22]
B335	$(1.70 \pm 0.3) \times 10^{-3}$	HDO/H_2O ($H_2{}^{18}O$)	[22]
L483	$(2.20 \pm 0.4) \times 10^{-3}$	HDO/H_2O ($H_2{}^{18}O$)	[22]

Note. — Note that not all measurements use the same method, but when the method is not HDO/H_2O, their values are translated into the equivalent HDO/H_2O by multiplying by a factor of 2 because HDO/H_2O = 2× D/H.

Methods References

[36] J. P. McMullin, B. Waters, D. Schiebel, W. Young, and K. Golap. CASA Architecture and Applications. In R. A. Shaw, F. Hill, and D. J. Bell, editors, *Astronomical Data Analysis Software and Systems XVI*, volume 376 of *Astronomical Society of the Pacific Conference Series*, page 127, October 2007.

[37] Richard Teague. richteague/keplerian_mask: Initial Release, 2020.

[38] Richard Teague and Daniel Foreman-Mackey. A Robust Method to Measure Centroids of Spectral Lines. *Research Notes of the American Astronomical Society*, 2:173, 2018.

[39] Richard Teague. Statistical Uncertainties in Moment Maps of Line Emission. *Research Notes of the American Astronomical Society*, 3(5):74, May 2019.

[40] Hsi-Wei Yen, Patrick M. Koch, Hauyu Baobab Liu, Evaria Puspitaningrum, Naomi Hirano, Chin-Fei Lee, and Shigehisa Takakuwa. Stacking Spectra in Protoplanetary Disks: Detecting Intensity Profiles from Hidden Molecular Lines in HD 163296. *Astrophys. J.*, 832(2):204, 2016.

[41] Adam Ginsburg, John Bally, Ciriaco Goddi, Richard Plambeck, and Melvyn Wright. A Keplerian Disk around Orion SrCI, a ~ 15 M $_\odot$ YSO. *Astrophys. J.*, 860(2):119, 2018.

[42] C. Brinch and M. R. Hogerheijde. LIME - a flexible, non-LTE line excitation and radiation transfer method for millimeter and far-infrared wavelengths. *Astron. Astrophys.*, 523:A25, 2010.

[43] T. Möller, C. Endres, and P. Schilke. eXtended CASA Line Analysis Software Suite (XCLASS). *Astron. Astrophys.*, 598:A7, 2017.

[44] Paul F. Goldsmith and William D. Langer. Population Diagram Analysis of Molecular Line Emission. *Astrophys. J.*, 517(1):209–225, 1999.

[45] H. M. Pickett, R. L. Poynter, E. A. Cohen, M. L. Delitsky, J. C. Pearson, and H. S. P. Müller. Submillimeter, millimeter and microwave spectral line catalog. *JQSRT*, 60(5):883–890, 1998.

[46] Y. C. Cheng, D. Bockelée-Morvan, M. Roos-Serote, J. Crovisier, V. Debout, S. Erard, P. Drossart, C. Leyrat, F. Capaccioni, G. Filacchione, M. L. Dubernet, and T. Encrenaz. Water ortho-to-para ratio in the coma of comet 67P/Churyumov-Gerasimenko. *Astron. Astrophys.*, 663:A43, 2022.

[47] Tetsuya Hama, Akira Kouchi, and Naoki Watanabe. Statistical ortho-to-para ratio of water desorbed from ice at 10 kelvin. *Science*, 351(6268):65–67, 2016.

[48] T. L. Wilson and R. Rood. Abundances in the Interstellar Medium. *ARA&A*, 32:191–226, 1994.

[49] K. Altwegg, H. Balsiger, M. Combi, J. De Keyser, M. N. Drozdovskaya, S. A. Fuselier, T. I. Gombosi, N. Hänni, M. Rubin, M. Schuhmann, I. Schroeder, and S. Wampfler. Molecule-dependent oxygen isotopic ratios in the coma of comet 67P/Churyumov-Gerasimenko. *Mon. Not. R. Astron. Soc.*, 498(4):5855–5862, 2020.

[50] F. L. Schöier, F. F. S. van der Tak, E. F. van Dishoeck, and J. H. Black. An atomic and molecular database for analysis of submillimetre line observations. *Astron. Astrophys.*, 432(1):369–379, 2005.

[51] A. Faure, L. Wiesenfeld, Y. Scribano, and C. Ceccarelli. Rotational excitation of mono- and doubly-deuterated water by hydrogen molecules. *Mon. Not. R. Astron. Soc.*, 420(1):699–704, 2012.

[52] Jonathan P. Williams and Lucas A. Cieza. Protoplanetary Disks and Their Evolution. *ARA&A*, 49(1):67–117, 2011.

[53] Fred C. Adams. The Birth Environment of the Solar System. *ARA&A*, 48:47–85, 2010.

[54] Steven J. Desch, Edward D. Young, Emilie T. Dunham, Yusuke Fujimoto, and Daniel R. Dunlap. Short-Lived Radionuclides in Meteorites and the Sun's Birth Environment. *arXiv e-prints*, page arXiv:2203.11169, 2022.

[55] Susanne Pfalzner and Kirsten Vincke. Cradle(s) of the Sun. *Astrophys. J.*, 897(1):60, 2020.

[56] R. Hagemann, G. Nief, and E. Roth. Absolute isotopic scale for deuterium analysis of natural waters. absolute d/h ratio for smow. *Tellus*, 22(6):712–715, 1970.

[57] John R. de Laeter, John Karl Böhlke, P. De Bièvre, H. Hidaka, H. S. Peiser, K. J. R. Rosman, and P. D. P. Taylor. Atomic weights of the elements. review 2000 (iupac technical report). *Pure and Applied Chemistry*, 75(6):683–800, 2003.

[58] Robert H. Brown, Dante S. Lauretta, Britney Schmidt, and John Moores. Experimental and theoretical simulations of ice sublimation with implications for the chemical, isotopic, and physical evolution of icy objects. *Planetary & Space Sci.*, 60(1):166–180, 2012.

[59] D. Bockelée-Morvan, D. Gautier, D. C. Lis, K. Young, J. Keene, T. Phillips, T. Owen, J. Crovisier, P. F. Goldsmith, E. A. Bergin, D. Despois, and A. Wootten. Deuterated Water in Comet C/1996 B2 (Hyakutake) and Its Implications for the Origin of Comets. *Icarus*, 133(1):147–162, 1998.

[60] Roland Meier, Tobias C. Owen, Henry E. Matthews, David C. Jewitt, Dominique Bockelee-Morvan, Nicolas Biver, Jacques Crovisier, and Daniel Gautier. A Determination of the HDO/H2O Ratio in Comet C/1995 O1 (Hale-Bopp). *Science*, 279:842, 1998.

[61] Erika L. Gibb, Boncho P. Bonev, Geronimo Villanueva, Michael A. DiSanti, Michael J. Mumma, Emily Sudholt, and Yana Radeva. Chemical Composition of Comet C/2007 N3 (Lulin): Another "Atypical" Comet. *Astrophys. J.*, 750(2):102, 2012.

[62] G. L. Villanueva, M. J. Mumma, B. P. Bonev, M. A. Di Santi, E. L. Gibb, H. Böhnhardt, and M. Lippi. A Sensitive Search for Deuterated Water in Comet 8p/Tuttle. *Astrophys. J. L.*, 690(1):L5–L9, 2009.

[63] D. Bockelée-Morvan, N. Biver, B. Swinyard, M. de Val-Borro, J. Crovisier, P. Hartogh, D. C. Lis, R. Moreno, S. Szutowicz, E. Lellouch, M. Emprechtinger, G. A. Blake, R. Courtin, C. Jarchow, M. Kidger, M. Küppers, M. Rengel, G. R. Davis, T. Fulton, D. Naylor, S. Sidher, and H. Walker. Herschel measurements of the D/H and $^{16}O/^{18}O$ ratios in water in the Oort-cloud comet C/2009 P1 (Garradd). *Astron. Astrophys.*, 544:L15, 2012.

[64] D. Hutsemékers, J. Manfroid, E. Jehin, J. M. Zucconi, and C. Arpigny. The $^{\{16\}}OH/^{18}OH$ and OD/OH isotope ratios in comet C/2002 T7 (LINEAR). *Astron. Astrophys.*, 490(3):L31–L34, 2008.

[65] N. Biver, D. Bockelée-Morvan, J. Crovisier, D. C. Lis, R. Moreno, P. Colom, F. Henry, F. Herpin, G. Paubert, and M. Womack. Radio wavelength molecular observations of comets C/1999 T1 (McNaught-Hartley), C/2001 A2 (LINEAR), C/2000 WM_1 (LINEAR) and 153P/Ikeya-Zhang. *Astron. Astrophys.*, 449(3):1255–1270, 2006.

[66] N. Biver, R. Moreno, D. Bockelée-Morvan, Aa. Sandqvist, P. Colom, J. Crovisier, D. C. Lis, J. Boissier, V. Debout, G. Paubert, S. Milam, A. Hjalmarson, S. Lundin, T. Karlsson, M. Battelino, U. Frisk, D. Murtagh, and Odin Team. Isotopic ratios of H, C, N, O, and S in comets C/2012 F6 (Lemmon) and C/2014 Q2 (Lovejoy). *Astron. Astrophys.*, 589:A78, 2016.

[67] D. C. Lis, N. Biver, D. Bockelée-Morvan, P. Hartogh, E. A. Bergin, G. A. Blake, J. Crovisier, M. de Val-Borro, E. Jehin, M. Küppers, J. Manfroid,

R. Moreno, M. Rengel, and S. Szutowicz. A Herschel Study of D/H in Water in the Jupiter-family Comet 45P/Honda-Mrkos-Pajdušáková and Prospects for D/H Measurements with CCAT. *Astrophys. J. L.*, 774(1):L3, 2013.

[68] Paul Hartogh, Dariusz C. Lis, Dominique Bockelée-Morvan, Miguel de Val-Borro, Nicolas Biver, Michael Küppers, Martin Emprechtinger, Edwin A. Bergin, Jacques Crovisier, Miriam Rengel, Raphael Moreno, Slawomira Szutowicz, and Geoffrey A. Blake. Ocean-like water in the Jupiter-family comet 103P/Hartley 2. *Nature*, 478(7368):218–220, 2011.

[69] Dariusz C. Lis, Dominique Bockelée-Morvan, Rolf Güsten, Nicolas Biver, Jürgen Stutzki, Yan Delorme, Carlos Durán, Helmut Wiesemeyer, and Yoko Okada. Terrestrial deuterium-to-hydrogen ratio in water in hyperactive comets. *Astron. Astrophys.*, 625:L5, 2019.

[70] Thomas Robitaille and Eli Bressert. APLpy: Astronomical Plotting Library in Python. Astrophysics Source Code Library, record ascl:1208.017, 2012.

[71] Astropy Collaboration, A. M. Price-Whelan, B. M. Sipőcz, H. M. Günther, P. L. Lim, S. M. Crawford, S. Conseil, D. L. Shupe, M. W. Craig, N. Dencheva, A. Ginsburg, J. T. VanderPlas, L. D. Bradley, D. Pérez-Suárez, M. de Val-Borro, T. L. Aldcroft, K. L. Cruz, T. P. Robitaille, E. J. Tollerud, C. Ardelean, T. Babej, Y. P. Bach, M. Bachetti, A. V. Bakanov, S. P. Bamford, G. Barentsen, P. Barmby, A. Baumbach, K. L. Berry, F. Biscani, M. Boquien, K. A. Bostroem, L. G. Bouma, G. B. Brammer, E. M. Bray, H. Breytenbach, H. Buddelmeijer, D. J. Burke, G. Calderone, J. L. Cano Rodríguez, M. Cara, J. V. M. Cardoso, S. Cheedella, Y. Copin, L. Corrales, D. Crichton, D. D'Avella, C. Deil, É. Depagne, J. P. Dietrich, A. Donath, M. Droettboom, N. Earl, T. Erben, S. Fabbro, L. A. Ferreira, T. Finethy, R. T. Fox, L. H. Garrison, S. L. J. Gibbons, D. A. Goldstein, R. Gommers, J. P. Greco, P. Greenfield, A. M. Groener, F. Grollier, A. Hagen, P. Hirst, D. Homeier, A. J. Horton, G. Hosseinzadeh, L. Hu, J. S. Hunkeler, Ž. Ivezić, A. Jain, T. Jenness, G. Kanarek, S. Kendrew, N. S. Kern, W. E. Kerzendorf, A. Khvalko, J. King, D. Kirkby, A. M. Kulkarni, A. Kumar, A. Lee, D. Lenz, S. P. Littlefair, Z. Ma, D. M. Macleod, M. Mastropietro, C. McCully, S. Montagnac, B. M. Morris, M. Mueller, S. J. Mumford, D. Muna, N. A. Murphy, S. Nelson, G. H. Nguyen, J. P. Ninan, M. Nöthe, S. Ogaz, S. Oh, J. K. Parejko, N. Parley, S. Pascual, R. Patil, A. A. Patil, A. L. Plunkett, J. X. Prochaska, T. Rastogi, V. Reddy Janga, J. Sabater, P. Sakurikar, M. Seifert, L. E. Sherbert, H. Sherwood-Taylor, A. Y. Shih, J. Sick, M. T. Silbiger, S. Singanamalla, L. P. Singer, P. H. Sladen, K. A. Sooley, S. Sornarajah, O. Streicher, P. Teuben, S. W. Thomas, G. R. Tremblay, J. E. H. Turner, V. Terrón, M. H. van Kerkwijk, A. de la Vega, L. L. Watkins, B. A.

Weaver, J. B. Whitmore, J. Woillez, V. Zabalza, and Astropy Contributors. The Astropy Project: Building an Open-science Project and Status of the v2.0 Core Package, September 2018.

[72] P. Greenfield, T. Robitaille, E. Tollerud, T. Aldcroft, K. Barbary, P. Barrett, E. Bray, N. Crighton, A. Conley, S. Conseil, M. Davis, C. Deil, N. Dencheva, M. Droettboom, H. Ferguson, A. Ginsburg, F. Grollier, H. Moritz Günther, C. Hanley, J. C. Hsu, W. Kerzendorf, R. Kramer, P. Lian Lim, D. Muna, P. Nair, A. Price-Whelan, D. Shiga, L. Singer, J. Taylor, J. Turner, J. Woillez, and V. Zabalza. Astropy: Community Python library for astronomy. *ASCL*, April 2013.

[73] Kristen M. Thyng, C. A. Greene, R. D. Hetland, H. M. Zimmerle, and S. F. DiMarco. True colors of oceanography: Guidelines for effective and accurate colormap selection. *Oceanography*, 29(3):9–13, September 2016.

Acknowledgments. This paper makes use of the following ALMA data: ADS/JAO.ALMA#2021.1.00186.S. ALMA is a partnership of ESO (representing its member states), NSF (USA) and NINS (Japan), together with NRC (Canada), MOST and ASIAA (Taiwan), and KASI (Republic of Korea), in cooperation with the Republic of Chile. The Joint ALMA Observatory is operated by ESO, AUI/NRAO and NAOJ. The National Radio Astronomy Observatory is a facility of the National Science Foundation operated under cooperative agreement by Associated Universities, Inc. This research made use of APLpy, an open-source plotting package for Python [70], Astropy (http://www.astropy.org), a community-developed core Python package for Astronomy [71, 72], the Python package spectral-cube (https://github.com/radio-astro-tools/spectral-cube), and matplotlib color maps from the Python package cmocean [73].

- Funding
  - John J. Tobin acknowledges support from the National Radio Astronomy Observatory and NASA Grant 80NSSC22K1159.
  - Merel van 't Hoff acknowledges support from the University of Michigan Society of Fellows.
  - Margot Leemker acknowledges support from the Dutch Research Council (NWO) grant 618.000.001.
  - Ewine van Dishoeck acknowledges support the Dutch Research Council (NWO), EU A-ERC grant No. 101019751 MOLDISK, and the Danish National Research Foundation "InterCat" grant (DNRF150).
  - Teresa Paneque-Carreño acknowledges support from the European Southern Observatory.
  - Patrick Sheehan acknowledges support from NSF grant AST-2001830.
  - Daniel Harsono is supported by Centre for Informatics and Computation in Astronomy (CICA) and grant number 110J0353I9 from the Ministry of Education of Taiwan. DH acknowledges support from the Ministry of Science of Technology of Taiwan through grant number 111B3005191.
  - Lucas Cieza acknowledges support from FONDECYT Grant 1211656 and the Millennium Nucleus YEMS, NCN2021-080, from ANID, Chile.
  - L. Ilsedore Cleeves gratefully acknowledges support from the David and Lucille Packard Foundation and NASA ATP 80NSSC20K0529.
  - Kenji Furuya acknowledges support from JSPS KAKENHI grant Nos. 20H05847 and 21K13967.
- Conflict of interest/Competing interests (check journal-specific guidelines for which heading to use)
  - The authors declare no competing financial interests.
- Availability of data and materials
  - The images used for analysis in the paper are available in the Harvard Dataverse repository (https://doi.org/10.7910/DVN/MDQJEU), along

with the reduction scripts used to process the ALMA visibility data and create images. Due to their size, the raw (and ALMA-pipeline-calibrated) visibility data are only available from the ALMA science archive (https://almascience.nrao.edu/aq/).

- Code availability
  - Codes used for are available in the Harvard Dataverse repository (https://doi.org/10.7910/DVN/MDQJEU), along with the ALMA images used for analysis. Documentation and requirements for various parts of the code are documented.
- Authors' contributions
  - John Tobin wrote the main text and led the data analysis.
  - Merel van 't Hoff assisted with the analysis and writing.
  - Margot Leemker assisted with the snowline analysis and writing
  - Teresa Paneque-Carreño assisted with the snowline analysis and writing.
  - Ewine van Dishoeck and Kenji Furuya contributed to the interpretation of results.
  - Magnus Persson created two of the figures and contributed to the interpretation of results.
  - L. Ilsedore Cleeves, Daniel Harsono, Patrick Sheehan and Lucas Cieza contributed to the interpretation of the results and the proofing of the manuscript.
  - All authors contributed to obtaining the observations.